

DISLOCATIONS AT LATTICE MISMATCHED WIDEGAP II-VI/GaAs
HETEROINTERFACES AS LASER LIGHT SCATTERERS:
EXPERIMENT AND THEORY

By

CHRISTOPHER M. ROULEAU

A DISSERTATION PRESENTED TO THE GRADUATE SCHOOL
OF THE UNIVERSITY OF FLORIDA IN PARTIAL FULFILLMENT
OF THE REQUIREMENTS FOR THE DEGREE OF
DOCTOR OF PHILOSOPHY

UNIVERSITY OF FLORIDA

1994

Dedicated to my father

ACKNOWLEDGEMENTS

I would like to express my sincere appreciation to Professor Robert M. Park, my supervisory committee chairman and dissertation advisor, for his constant professional guidance, support, and encouragement during my research and studies. The knowledge and skills that he shared greatly enhanced my learning experience.

I would also like to thank Drs. Paul H. Holloway, Joseph H. Simmons, Kevin S. Jones, and David B. Tanner for serving as my doctoral committee. Their assistance and interest in my work are gratefully appreciated.

I am also indebted to Christopher J. Santana, my colleague, whose expertise in transmission electron microscopy sample preparation and analysis was instrumental in developing this dissertation.

Many thanks are also due to Dr. James V. Masi, professor of Electrical Engineering at Western New England College, who, as my undergraduate professor and mentor, encouraged me always to "keep the spirit and curious mind."

A special word of thanks is also extended to my best friend and wife, Mary, who provided support and encouragement throughout my graduate studies.

TABLE OF CONTENTS

	<u>page</u>
ACKNOWLEDGEMENTS	iii
LIST OF TABLES	vii
LIST OF FIGURES	viii
ABSTRACT	xiii
CHAPTERS	
1 INTRODUCTION	1
Background and Motivation	1
Outline of Dissertation Contents	4
2 GaAs SUBSTRATE CLEANING FOR HETEROEPITAXY	6
Background	6
Experimental Apparatus	7
MBE System Configuration	7
Characterization of Optical System	10
UHV Compatible rf Plasma Source	12
Precision Substrate Temperature Calibration	21
<i>In Situ</i> GaAs Surface Cleaning	25
Conclusions	31
3 LASER LIGHT SCATTERING DURING ZnSe/GaAs HETEROEPITAXY	33

Background	33
Experimental Apparatus	34
MBE Growth Chamber	34
Laser Probe Apparatus	36
Heteroepitaxy	37
Particle Contamination Considerations	37
<i>Ex Situ</i> Substrate Preparation	40
Laser Light Scattering from Typical Epilayers	41
Laser Light Scattering from Very Thick Epilayers	47
Structural Characterization	51
Lattice Mismatch Sensitivity	57
Conclusions	59
4 THEORY	60
The Role of Electric Microfields	60
Deformation Potential	61
Charged Dislocation Potential	64
Piezoelectric Potential	66
The Linear Electro-optic Effect	71
Conclusions	73
5 CONCLUSIONS	74
REFERENCE LIST	79
BIOGRAPHICAL SKETCH	83

LIST OF TABLES

<u>Table</u>	<u>page</u>
1 ZnSe material parameters necessary to evaluate the scalar coefficient of the microelectric field induced by the deformation potential (Eq. 1).	65
2 ZnSe material parameters necessary to evaluate the scalar coefficient of the microelectric field induced by the charged dislocation potential (Eq. 2). GaAs material parameters are used in some cases (denoted by a superscript a) since values for ZnSe were unavailable.	68

LIST OF FIGURES

<u>Figure</u>	<u>page</u>
1 Schematic of the custom-designed molecular beam epitaxy system showing conventional effusion sources, reflection high energy electron diffraction system, and ultra-high vacuum compatible rf plasma source fitted with a precision leak valve and gas line for hydrogen. Also illustrated is a schematic of the experimental setup used to characterize the surface morphology of GaAs during cleaning by recording the scattered HeNe laser light (or lack thereof) during the cleaning procedures. The geometry indicated in the figure provides for simultaneous reflection high energy electron diffraction analysis as shown.	9
2 Schematic of the apparatus employed to characterize the camera-based detection system transfer function at 632.8nm.	11
3 Camera-based detection system transfer function recorded at 632.8nm.	13
4 Schematic of the ultra-high vacuum compatible rf plasma source used to generate a flux of atomic hydrogen. Typical operating conditions were 320W forward power (<2W reflected) with an equilibrium background pressure of H in the growth chamber maintained at 5×10^{-6} mbar.	15
5 Schematic of the experimental setup used to record the optical emission spectrum associated with the hydrogen plasma created in the discharge region of the ultra-high vacuum compatible rf plasma source indicated in Figs. 1 and 4.	16

11	Representative reflection high energy electron diffraction patterns recorded from atomically clean GaAs surfaces resulting from conventional thermal treatment and the combined thermal/H-atom treatment and after removal of the H-atom flux, (a), (b), and (c), respectively.	29
12	Schematic of the experimental setup used to record elastically scattered laser light (ELLS) and specularly reflected laser light during the molecular beam epitaxial growth of widegap II-VI/GaAs heterostructures.	35
13	Dark-field optical micrographs indicating typical particle densities resulting from cleaving, gas burst cleaning and continuous (~5 seconds) gas flow cleaning, (a), (b), and (c), respectively. Note: the cleave line runs horizontally through the micrographs.	39
14	Intensity of scattering occurring near the ZnSe/GaAs (GaAs supplied by American Xtal Technology) heterointerface as a function of ZnSe epitaxial deposition time and layer thickness. Also included in the figure is a laser reflection interferogram to compare signal phasing.	42
15	Intensity of scattering occurring near the ZnSe/GaAs (GaAs supplied by Sumitomo Electric) heterointerface as a function of ZnSe epitaxial deposition time and layer thickness. Also included in the figure is a laser reflection interferogram to compare signal phasing.	44
16	A ray model illustrating the employment of a HeNe laser beam to probe the ZnSe/GaAs heterointerface during epitaxial deposition. Defect evolution gives rise to a scattered signal which was detected and quantified using the apparatus shown in Fig. 12.	45
17	Intensity of scattering occurring near the ZnSe/GaAs (GaAs supplied by Sumitomo Electric) heterointerface as a function of ZnSe epitaxial deposition time and layer thickness for a very	

thick (~30 μ m) film. Also included in the figure is a laser reflection interferogram. Note that the signals are in phase for this case.	48
18 Plan-view scanning electron micrographs (of ZnSe/GaAs) indicating the surface features present on a thin (~60nm), thick (~840nm) and very thick (~30 μ m) film, (a), (b), and (c), respectively.	50
19 A matrix of plan-view transmission electron micrographs (70,000X) comparing and contrasting the defects present near the ZnSe/GaAs heterointerface as a function of film thickness (row 1 through 6 = 60, 120, 300, 360, 600, and 840nm, respectively) and substrate type (column 1 and 2 = American Xtal Technology and Sumitomo Electric, respectively).	52
20 Recompilation of laser scattering data presented in Figs. 14 and 15 which compares and contrasts the laser scattering from an epilayer grown on an American Xtal Technology GaAs wafer to that of an epilayer grown on a Sumitomo Electric GaAs wafer. Epilayers of the thicknesses indicated by the vertical arrows were targeted for structural characterization. Note the difference in the detectable onset (in terms of layer thickness) of scattering.	54
21 A representative selected area diffraction pattern and high-resolution cross-sectional transmission electron micrograph which are indicative of the crystallinity and defect type present in the epilayers represented by the micrographs shown in Figs. 19(g)-(i).	56
22 Elastically scattered laser light data recorded in real-time during the deposition of ZnSe/GaAs and ZnTe/GaAs heterostructures. The lattice-mismatches indicated in the figure correspond to room temperature lattice-mismatches. Note the difference in detectable onset (in terms of layer thickness) of scattering.	58

23	A cartesian mesh plot of the function presented in Eq. 1 showing the electric field intensity due to the deformation potential as a function of position around the dislocation core. The dislocation core lies along the electric field intensity axis.	63
24	A cartesian mesh plot of the function presented in Eq. 2 showing the electric field intensity due to a charged dislocation as a function of position around the dislocation core. The dislocation core lies along the electric field intensity axis.	67
25	A cartesian mesh plot of the function presented in Eq. 3 showing the piezoelectric field intensity as a function of position around the dislocation core. The dislocation core lies along the electric field intensity axis.	70

Abstract of Dissertation Presented to the Graduate School
of the University of Florida in Partial Fulfillment of the
Requirements for the Degree of Doctor of Philosophy

DISLOCATIONS AT LATTICE MISMATCHED WIDEGAP II-VI/GaAs
HETEROINTERFACES AS LASER LIGHT SCATTERERS:
EXPERIMENT AND THEORY

By

Christopher M. Rouleau

August, 1994

Chairperson: Robert M. Park

Major Department: Materials Science and Engineering

This work concerned an investigation using real-time *in situ* electron and laser beam probes of GaAs substrate surfaces intended for epitaxy and of the strain relief process associated with growing ZnSe/GaAs heterostructures by the molecular beam epitaxy technique.

An *in situ* GaAs surface cleaning process was developed using a remote H atom flux supplied by an ultra-high vacuum compatible rf plasma source. GaAs surface cleanliness and morphology were monitored *in situ* and in real-time using reflection high energy electron diffraction (RHEED) and an elastic laser light scattering (ELLS) technique, respectively.

From RHEED observations, GaAs surfaces were found to clean readily at temperatures near 350°C using the H atom treatment as opposed to the conventional thermal treatment, which requires temperatures near 600°C. The atomically clean GaAs surfaces were found to be specular (ELLS observations) when prepared using the H atom treatment, and hydrogen stabilization of the surface is suggested from the RHEED observations.

In terms of heteroepitaxial growth, a near-normal incidence HeNe laser probe was employed that generated both a specularly reflected laser light signal and an ELLS signal beyond a critical epilayer thickness. It was determined that the ELLS signal was generated locally at the ZnSe/GaAs heterointerface, as opposed to the free-surface, based on the observation of a π phase difference between the two signals, which were monitored simultaneously. It is postulated, based on a theoretical model, that dislocations arising at the ZnSe/GaAs heterointerface can act as laser light scatterers due to strong microelectric fields that surround the defects and that perturb the refractive index in a localized manner.

Postgrowth, *ex situ* transmission electron microscopy was performed on a selection of heterostructures, and a high degree of correlation was found between the optical data recorded during film growth and the nature of the

defect structure present near the heterointerface, which strongly supports the theoretical model.

CHAPTER 1 INTRODUCTION

Background and Motivation

The quality of a heteroepitaxial structure, which for the purposes of this work is a system comprising an interface between two dissimilar materials, namely a film material and a substrate material, is critically dependent upon the nature of the substrate surface prior to epitaxy and the degree of lattice parameter and thermal expansion coefficient mismatch between the two materials. Photonic devices are particularly sensitive to the presence of structural defects that arise as a consequence of nonideal substrate surface preparation and/or significant lattice parameter and thermal expansion coefficient mismatches.

Traditionally, the results of mismatched heteroepitaxy and/or nonideal surface preparation are revealed by performing postgrowth characterization of suitably processed samples using techniques such as transmission electron microscopy and high resolution x-ray diffraction, for instance. However, in addition to being time consuming and expensive, such postgrowth

characterization techniques cannot readily distinguish between sources of defects (substrate surface irregularities, lattice mismatch strain, etc.). The work of this dissertation focused on addressing independently the nature of a substrate surface and the issue of plastic deformation at a mismatched heterointerface. The subject material system concerned ZnSe/GaAs heterostructures.

The primary motivation of the project was to develop *in situ* optical probes that could be used to assess wafer quality and to study strain relief in real-time during epitaxial growth. An objective was to correlate optical data recorded during film growth with structural defect analysis data obtained postgrowth. Another issue of major concern in this project was to develop an *in situ* cleaning technique for GaAs that would provide an ideal surface for epitaxy, namely a contamination-free, stoichiometric, and atomically smooth surface. Again, the idea was to develop an *in situ* probe that would be capable of providing useful information on the nature of the substrate surface during *in situ* processing.

Real-time, *in situ* monitoring techniques, in general, represent very powerful capabilities with regard to process diagnosis and control. For example, with respect to molecular beam epitaxy (MBE), reflection high

energy electron diffraction (RHEED) is employed on a routine basis to determine surface reconstruction and to assess the quality of substrate surfaces and subsequent epilayers. Recently, however, optical techniques have become increasing popular due to their noninvasive nature and their ability to provide information on properties other than crystal structure. Ellipsometry, for instance, has far-reaching capabilities that include real-time, *in situ* monitoring and control of alloy composition, growth rate, and substrate temperature during MBE deposition.¹⁻³ Also, real-time, *in situ* monitoring of the free carrier concentration in doped ZnSe films by quantitative cathodoluminescence analysis has been reported.⁴ In addition, Lavoie et al.⁵ have reported real-time, *in situ* monitoring of the GaAs oxide desorption process prior to epitaxial growth by measuring the intensity of elastically scattered laser light at the GaAs surface and have concluded that there is an associated roughening of the GaAs surface. Also along these lines, Piddock et al.^{6,7} and Robbins et al.⁸ have performed similar elastic laser light scattering measurements during Si MBE and SiGe/Si heteroepitaxy, respectively, and have concluded that changes in the surface morphology occurring during layer processing can conveniently be monitored and characterized by such means.

As will be described in the following chapters, we have developed our own optical probing methods to study in real-time the ZnSe/GaAs heteroepitaxial system, and it will be demonstrated that heterointerface defects, rather than surface irregularities, result in laser light scattering following plastic deformation in this particular material system. The observation of heterointerface laser light scattering is novel.

Outline of Dissertation Contents

The dissertation is composed of 5 chapters. Chapter 1 presents the background and motivation for the project.

Chapter 2 pertains to GaAs substrate cleaning for epitaxy and is subdivided into three main sections describing experimental apparatus, conventional thermal and combined thermal/H-atom cleaning studies, and relevant conclusions.

Chapter 3 pertains to ZnSe/GaAs heteroepitaxy and is subdivided into three main sections describing experimental apparatus, results of optical monitoring during heteroepitaxy under various conditions, and relevant conclusions.

Chapter 4 presents a theoretical model to account for the observed laser light scattering during ZnSe/GaAs epilayer growth, and chapter 5 summarizes the important findings of the research effort.

CHAPTER 2

GaAs SUBSTRATE CLEANING FOR HETEROEPITAXY

Background

The conventional procedure employed in cleaning GaAs substrates for epitaxy, which involves wet chemical processing followed by *in situ* heating prior to MBE growth, has been extensively studied, for example, by Contour et al.⁹ and Vasquez, Lewis and Grunthaner,¹⁰ and by authors cited in these references. Problems with this technique, however, include the requirement of a processing temperature in the vicinity of 600°C and the fact that the resultant GaAs surface can be rough on the atomic level.

In recent years, various novel cleaning procedures have been reported, including *in situ* chemical etching of GaAs by gaseous HCl,¹¹ photochemical processing of GaAs,¹² and preliminary work on the removal of the native oxides from the GaAs surface using various hydrogen plasmas.¹³⁻¹⁷ These plasma techniques have been applied with varying degrees of success depending on the type of plasma and surface temperature required. Unfortunately, these techniques have problems since H rapidly decomposes

GaAs and the fast particles and ions generated in some of the plasmas degrade surface electronic properties.¹⁸

In an effort to explore new soft procedures, Schaefer et al.,¹⁹ Petit et al.,²⁰ and Petit and Houzay²¹ recently reported on the interaction of atomic hydrogen, generated by dissociating H₂ via a hot filament, with the GaAs native oxides, concluding that the oxides can be reduced to a large extent by such a technique whilst limiting As desorption, GaAs decomposition, and dopant deactivation.

With these reports in mind, one of the objectives of this work was to investigate the use of an ultra-high vacuum (UHV) compatible rf plasma source to generate an atomic hydrogen flux for GaAs oxide reduction. We had previously developed such an rf plasma source for doping ZnSe p-type via an atomic nitrogen beam.²²

Experimental Apparatus

MBE System Configuration

Growth chamber. The experiments were carried out in a custom-designed MBE system equipped with conventional effusion sources for Zn, Se, and Te, a RHEED system for assessing substrate surface quality, and a

UHV compatible rf plasma source manufactured by Oxford Applied Research (Oxfordshire, UK), which was previously used as a source of nitrogen atoms for doping ZnSe p-type.²² In addition to these conventional components, the MBE chamber was also configured with a laser probe apparatus as illustrated in Fig. 1.

Laser probe apparatus. The apparatus consisted of a 1mW HeNe laser ($\lambda=632.8\text{nm}$) mounted outside the MBE growth chamber, the laser beam being directed through a viewport towards the substrate, which was mounted on a heated Mo substrate holder. The detector/amplifier stage of the apparatus consisted of a color, charged coupled device (CCD) video camera (with a light intensity sensitivity of 2.5lux) and a color video monitor. The camera was mounted outside the system on its own viewport, its optical axis lying along the sample normal, which was 10° away from the optical axis of the incident laser beam. This particular geometry provided for simultaneous RHEED analysis as indicated in the figure. The camera was focused on the substrate surface, and the visible spot arising from elastically scattered laser light (ELLS) due to surface morphology changes (roughening) was displayed on the video monitor at a magnification of 3-4X. The intensity of the scattered laser light was quantified by attaching a Si wide-area photodiode

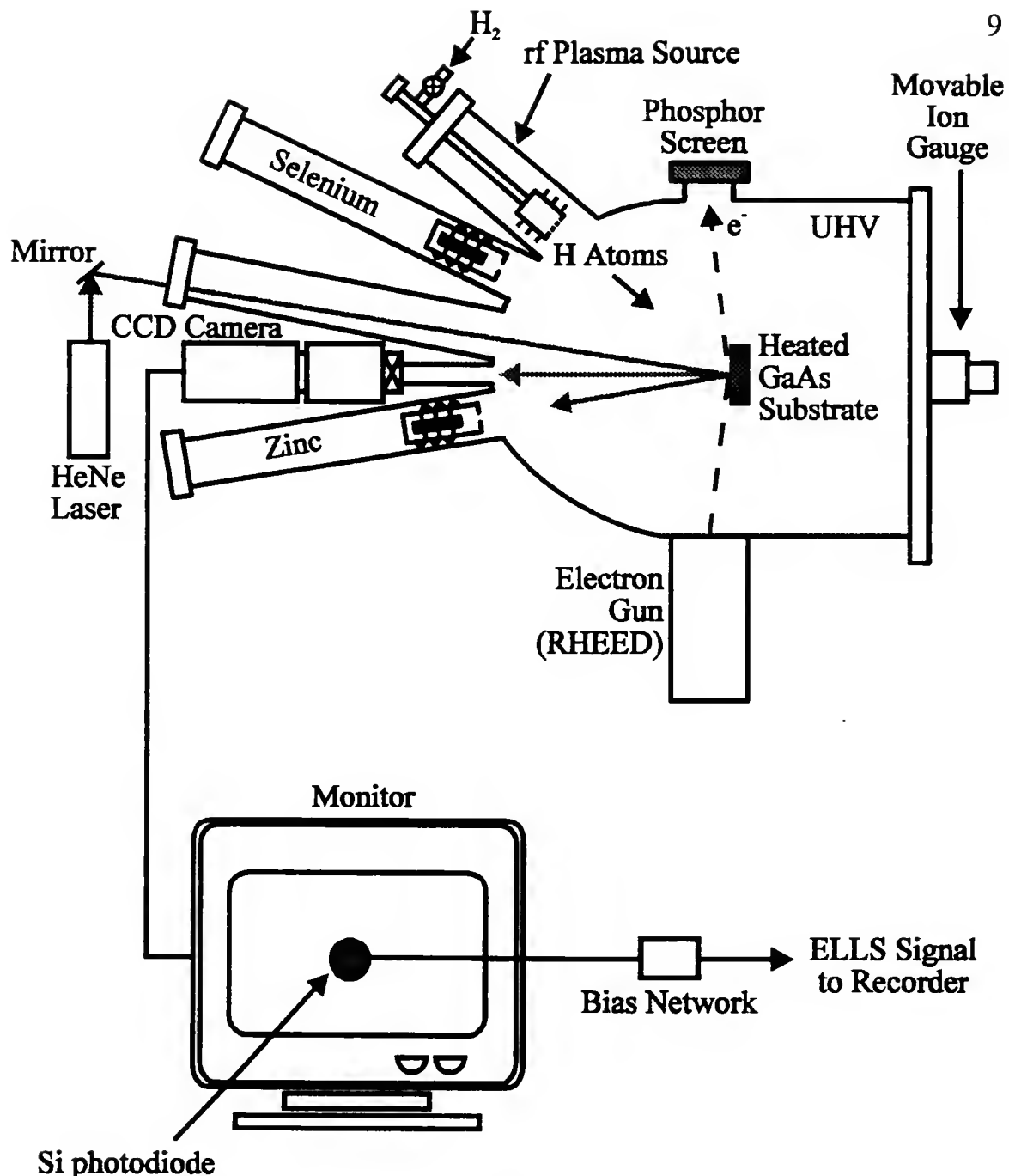


Figure 1 Schematic of the custom-designed molecular beam epitaxy system showing conventional effusion sources, reflection high energy electron diffraction system, and ultra-high vacuum compatible rf plasma source fitted with a precision leak valve and gas line for hydrogen. Also illustrated is a schematic of the experimental setup used to characterize the surface morphology of GaAs during cleaning by recording the scattered HeNe laser light (or lack thereof) during cleaning procedures. The geometry indicated in the figure provides for simultaneous reflection high energy electron diffraction analysis as shown.

to the monitor's cathode ray tube (CRT) over the image of the spot, and the output voltage from its respective bias network was recorded as a function of time. It should be noted that the specular reflection was not utilized in this experiment.

Characterization of Optical System

Due to the unorthodox nature of the detection system employed in quantifying the intensity of elastically scattered laser light, it was deemed important to characterize the transfer function of the camera-based detection system, and the apparatus illustrated schematically in Fig. 2 was employed to perform this task. A tungsten lamp, lens, diffuser, and laser line filter combination was used to provide a monochromatic ($\lambda=632.8\text{nm}$) input signal whose intensity could be varied over a wide dynamic range. To quantify the intensity of light entering the camera system from the source, a beam splitter was placed in front of the camera lens to direct a portion of the input light towards a photodiode. The output voltage from the bias network associated with this photodiode was then proportional to the light intensity directed into the camera-based detection system. The system transfer function was deduced by comparing the output voltage from the other bias network with

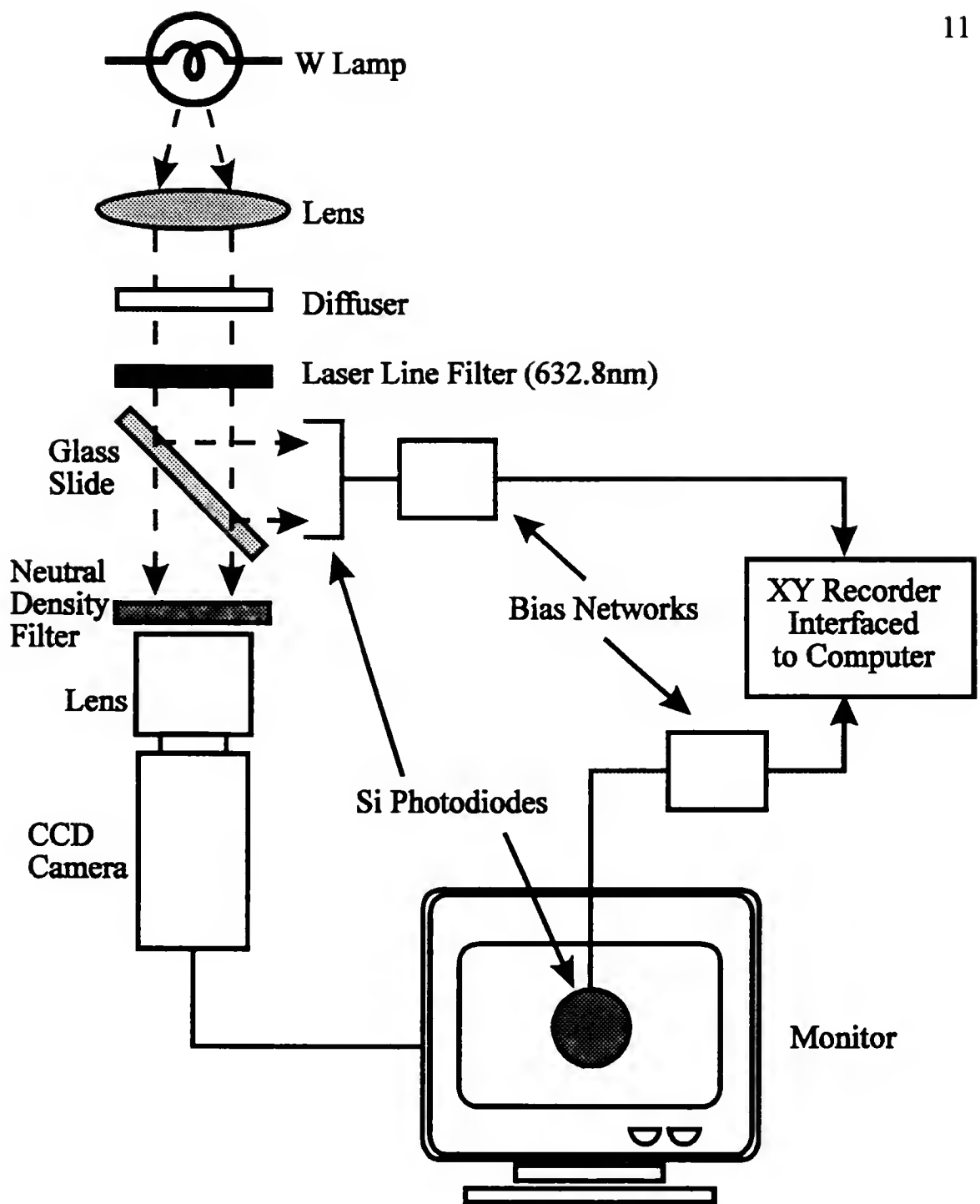


Figure 2 Schematic of the apparatus employed to characterize the camera-based detection system transfer function at 632.8nm.

the input voltage, both intensities being recorded simultaneously with an XY recorder as indicated in the figure.

As illustrated in Fig. 3, the detection system exhibited a threshold beyond which a linear regime was observed. As the input intensity increased, the system responded in an increasingly nonlinear fashion as indicated in the figure. This was most likely due to the automatic gain control circuitry in both the CCD camera and the monitor. For further increases in input intensity, the system response was clamped, presumably in response to the saturation of the CCD array. Using this information, attempts were made throughout the experiments to keep the detection system in a regime where clamping did not occur. The system was, however, allowed to operate in the linear/nonlinear regimes so that a reasonable degree of dynamic range could be achieved.

UHV Compatible rf Plasma Source

In this work, the rf plasma source was fitted with an additional precision leak valve and hydrogen gas line (see Fig. 1), which allowed for the production of a hydrogen or a nitrogen radical beam depending on the

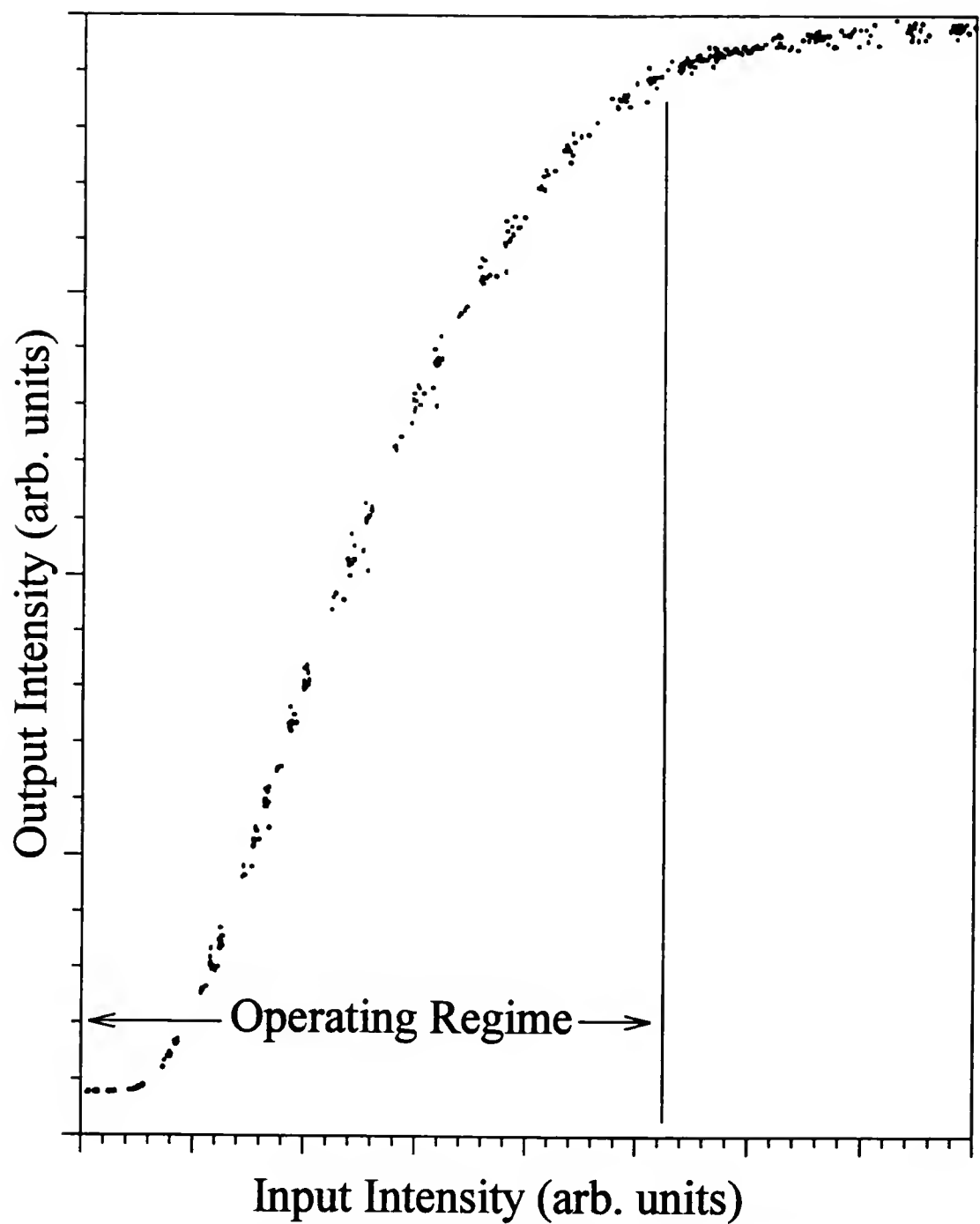


Figure 3 Camera-based detection system transfer function recorded at 632.8nm.

gas introduced into the discharge chamber. Figure 4 shows a schematic of the rf plasma source as configured for hydrogen atom production.

Coupled rf (13.56MHz) energy is manually adjusted with a capacitive power matching unit so that the reflected power is usually less than or approximately 2W. Gas flow into the pyrolytic boron nitride (PBN) discharge chamber is controlled via a UHV compatible precision leak valve. A water-cooled rf induction coil surrounds the discharge chamber, and a silicon-diode-based optical emission monitor provides a measure of plasma intensity inside the discharge chamber. A PBN multi-aperture disk positioned at the end of the discharge chamber allows the hydrogen species to exit into the growth chamber as shown. The source of hydrogen was a conventional high pressure (~2000psig) cylinder of ultra-high-purity (99.999% H₂ and <3ppm H₂O) hydrogen, which was regulated to 10psig before being introduced into the precision leak valve.

Characteristic hydrogen spectrum. To examine the species in the plasma, optical emission spectroscopy (OES) was performed using the apparatus shown in Fig. 5. Following removal of the optical emission monitor (see Fig. 4), light from the plasma region was guided into the 25 μ m slit of the monochromator using a mirror and a lens. The diffraction grating

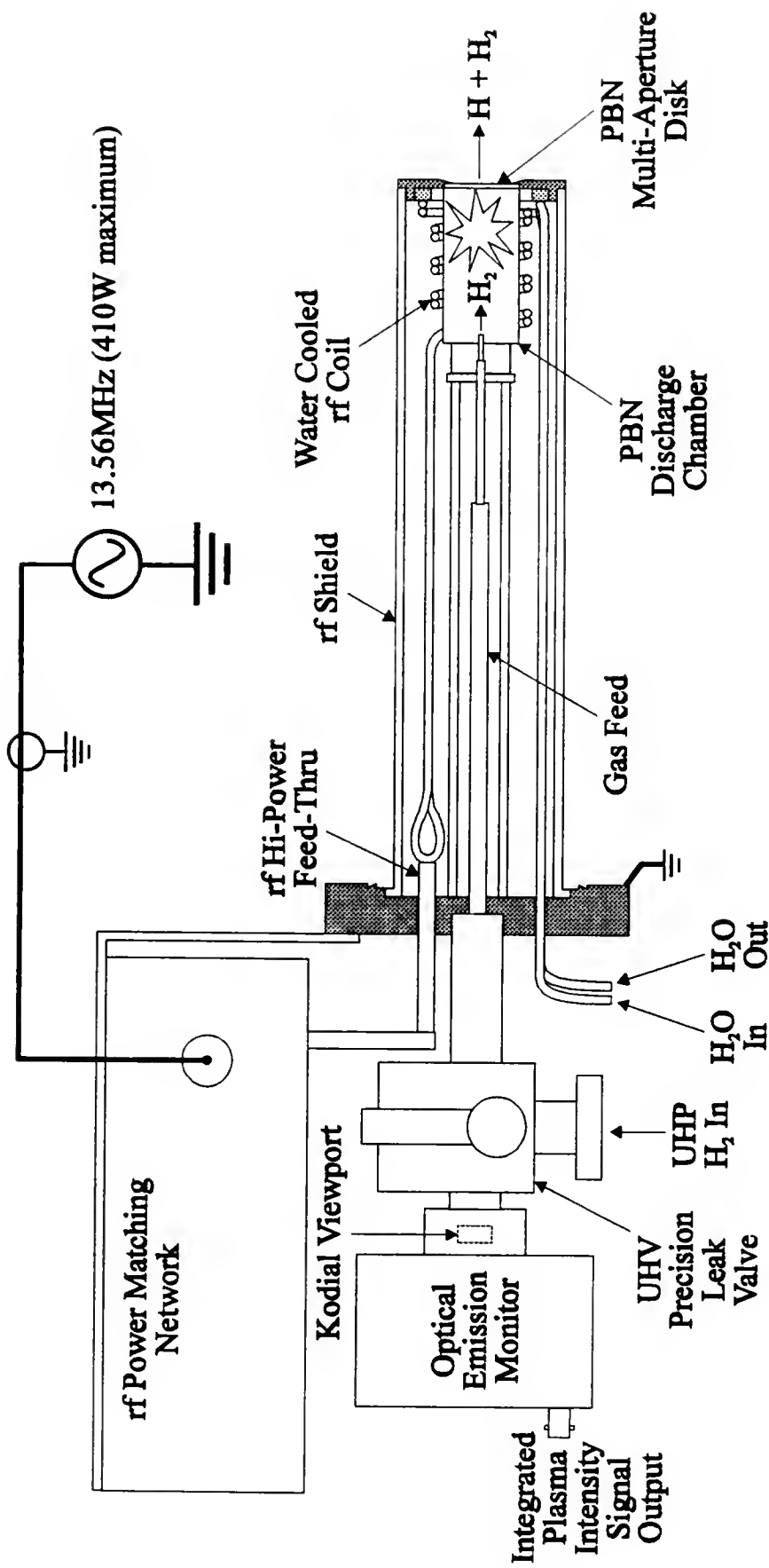


Figure 4 Schematic of the ultra-high vacuum compatible rf plasma source used to generate a flux of atomic hydrogen. Typical operating conditions were 320W forward power (<2W reflected) with an equilibrium background pressure of H in the growth chamber maintained at 5×10^{-6} mbar.

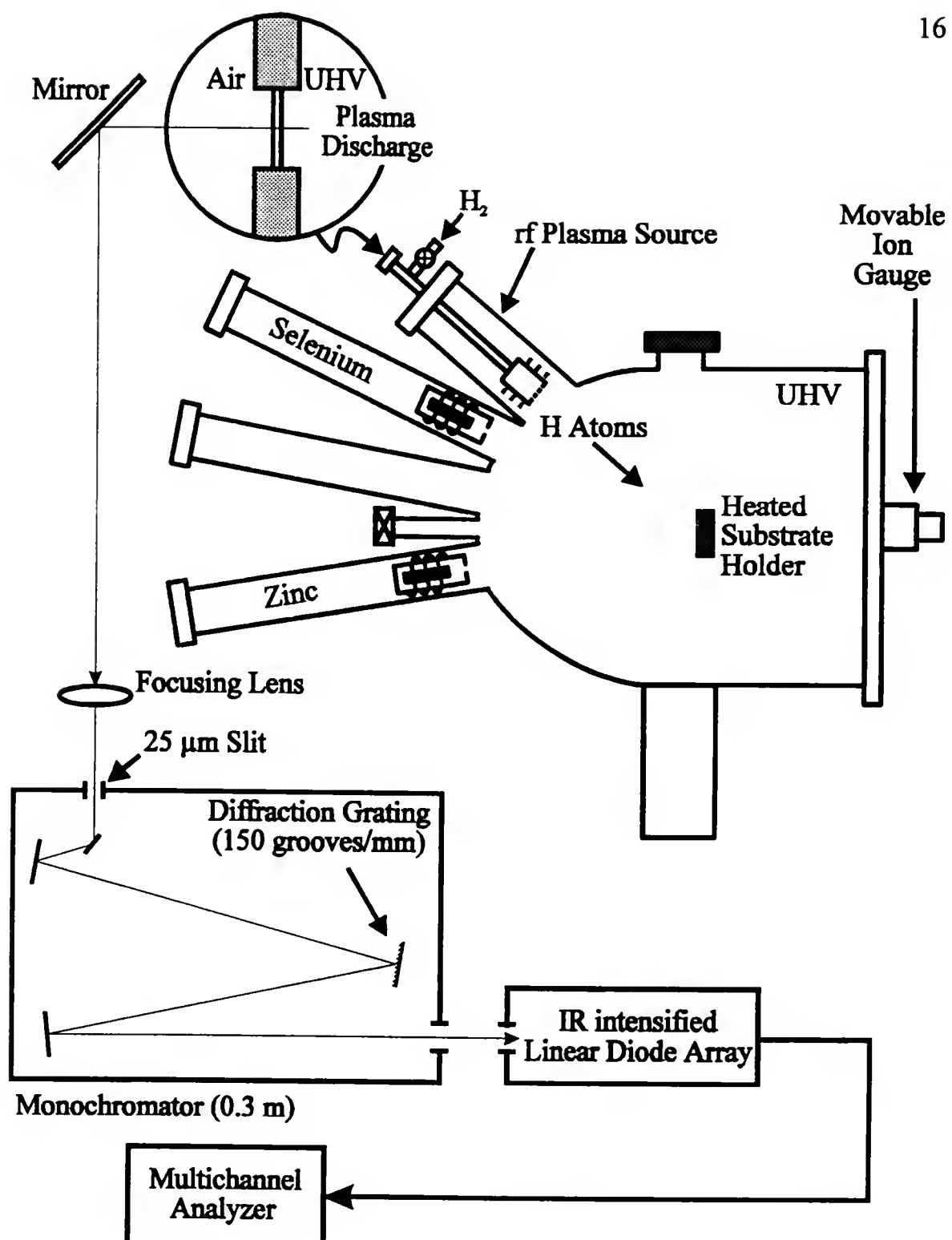


Figure 5 Schematic of the experimental setup used to record the optical emission spectrum associated with the hydrogen plasma created in the discharge region of the ultra-high vacuum compatible rf plasma source indicated in Figs. 1 and 4.

(150 grooves/mm) contained in the monochromator dispersed the light onto a linear array of 760 IR-intensified silicon diodes. A multichannel analyzer converted the signals from the diode array into an emission spectrum.

Figure 6 illustrates a typical optical emission spectrum recorded from the hydrogen plasma region under standard operating conditions of the source. The rf power used to create the discharge was 320W, while the equilibrium background pressure of hydrogen in the MBE growth chamber was 5×10^{-6} mbar. The emission spectrum shown in Fig. 6 is similar to that reported by Sugata et al.¹⁵ (see Fig. 6 inset) who employed an electron cyclotron resonance (ECR) microwave discharge source, although in the present spectrum only atomic hydrogen lines are evident as suggested by the featureless baseline and strong emission lines commonly associated with electronic transitions in the neutral hydrogen atom. The emission lines designated H _{α} , H _{β} , and H _{γ} , represent the first three lines in the characteristic visible spectrum (Balmer series) of the hydrogen atom,²³ and consequently, atomic hydrogen would seem to compose a significant fraction of the flux emanating from the rf plasma source.

Hydrogen spectrum evolution. To further explore the operating characteristics of the rf plasma source whilst configured for hydrogen atom

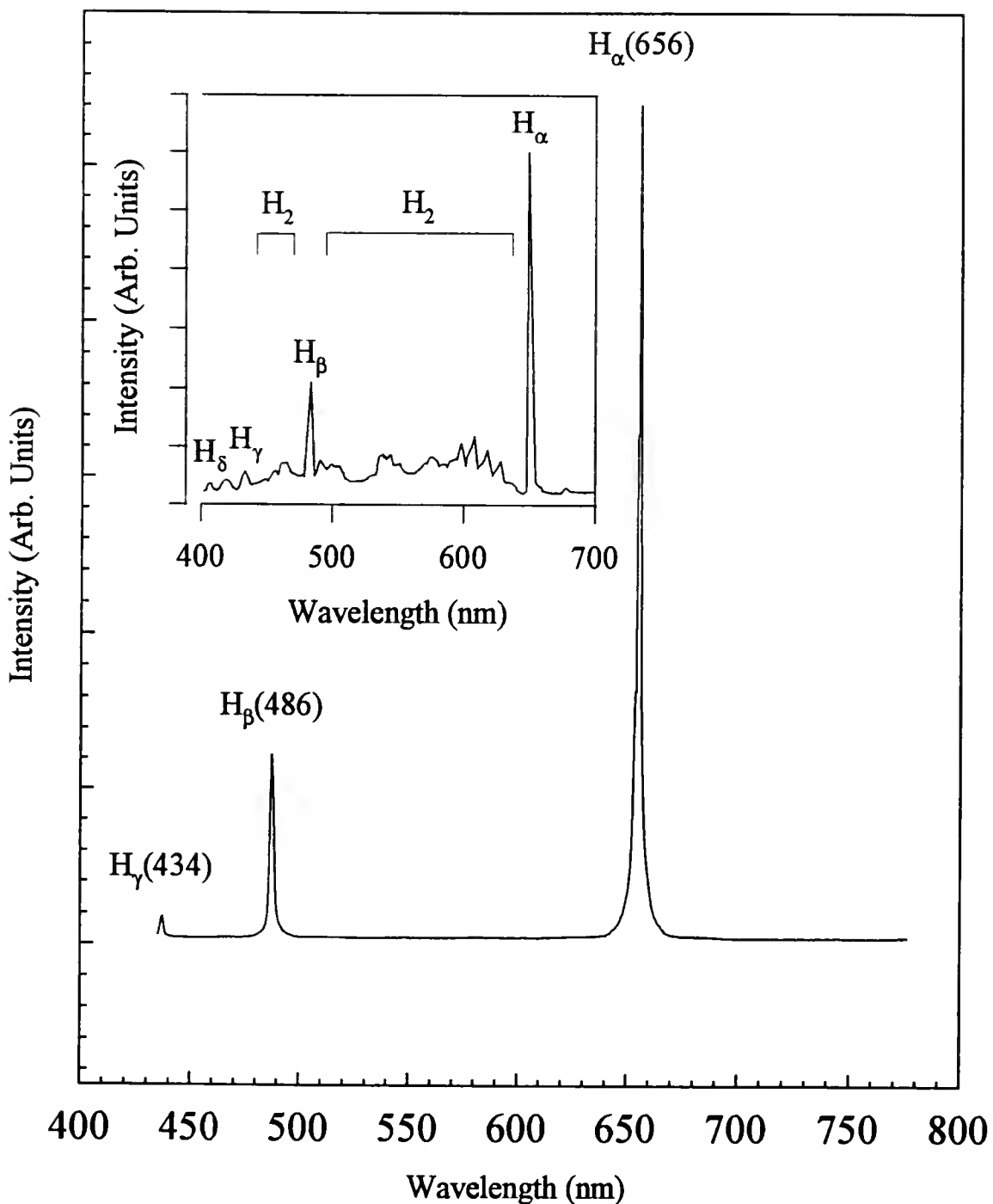


Figure 6 A characteristic optical emission spectrum recorded from the hydrogen plasma region of the ultra-high vacuum compatible rf plasma source illustrating emission lines characteristic of atomic hydrogen. The rf power used to create the discharge was 320W (<2W reflected) while an equilibrium background pressure of hydrogen in the molecular beam epitaxy growth chamber of 5×10^{-6} mbar was maintained. Inset shows an emission spectrum from an ECR plasma source (from Sugata et al.¹⁵).

production, time-dependent OES was performed over a period of 14 days following attainment of the hydrogen plasma shown in Fig. 6. More specifically, the plasma was ignited on selected days and stabilized, an optical emission spectrum was recorded, and then the rf plasma source was shut down. Figure 7 is a compilation of those results, and it should be noted that all spectra are the same scale.

As indicated in Fig. 7(a), the spectrum recorded on day 13 indicated a lack of the characteristic H_{γ} and H_{β} lines and a broadening of the H_{α} line. New features were also present near 580, 755, and 780nm. After a mechanical pump was used to evacuate the hydrogen feed line for 5 minutes and the line was back-filled with hydrogen, Fig. 7(b) indicated a return of the characteristic H_{γ} and H_{β} lines and a corresponding narrowing of the H_{α} line. The features near 580 and 755nm, however, were not present. After 24 hours, however, the features near 580 and 755nm returned as indicated in the figure (see Fig. 7(c)). The optimum spectrum, as indicated by characteristic hydrogen emission lines and a featureless baseline, is represented by Fig. 7(d) and was obtained by evacuating and back-filling the hydrogen feed line several times. As a result, this procedure (i.e., evacuate/back-fill the line several times prior to using the source) was

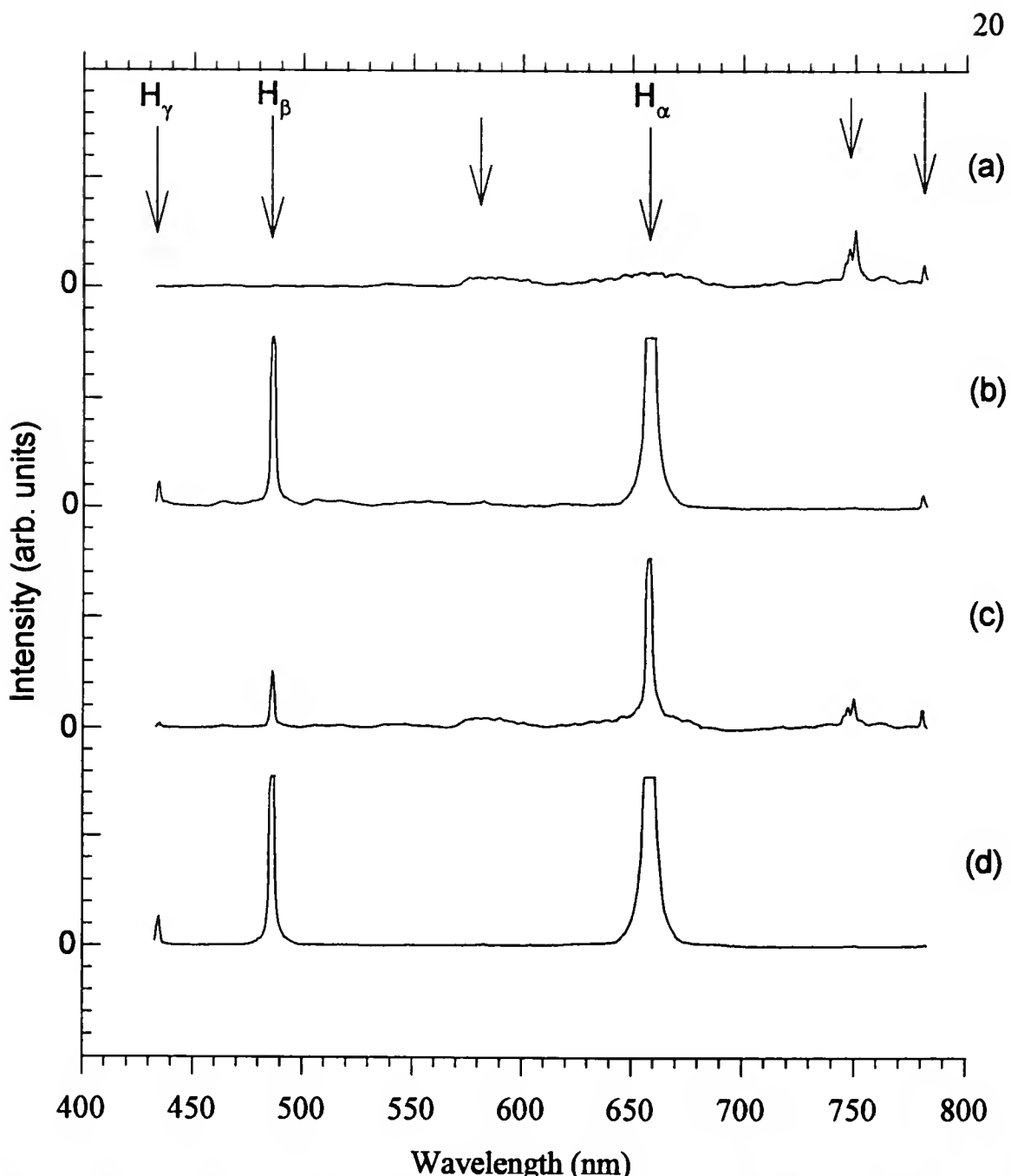


Figure 7 Evolution of the characteristic optical emission spectrum recorded from the hydrogen plasma region of the ultra-high vacuum compatible rf plasma source as a function of time. Spectrum (a) was recorded 13 days after that of Fig.6. Spectrum (b) was recorded after evacuating the H feed line with a pump for 15 minutes and then back-filling the line with H. Spectrum (c) was recorded 24 hours later and spectrum (d) was recorded after evacuating and back-filling the H feed line several times. Note: the source was on during recording of the spectra and off otherwise.

adopted as a standard operating procedure for all future experiments in which the rf plasma source was employed.

It is interesting to note that the positions of the additional features present in Figs. 7(a) and (c) correspond well with emission band locations associated with active nitrogen,²² which is not surprising since the source had previously been used with nitrogen²⁴ and therefore it is likely the most probable contaminant along with air in the feed line.

Precision Substrate Temperature Calibration

Before the oxide desorption experiments, the laser scattering apparatus was employed to calibrate precisely the temperature at the surface of the substrate by monitoring the formation of a eutectic from selected binary alloys. The melting temperature of In was also used as a low temperature calibration point.

As shown in Fig. 8, the heated substrate holder, having an integral thermocouple (T/C) that was displaced from the substrate, was tilted such that the angle of incidence of the impinging laser beam was 70° since it was determined that this angle provided the largest change in the intensity of laser light scattered in the direction of the detection system upon eutectic

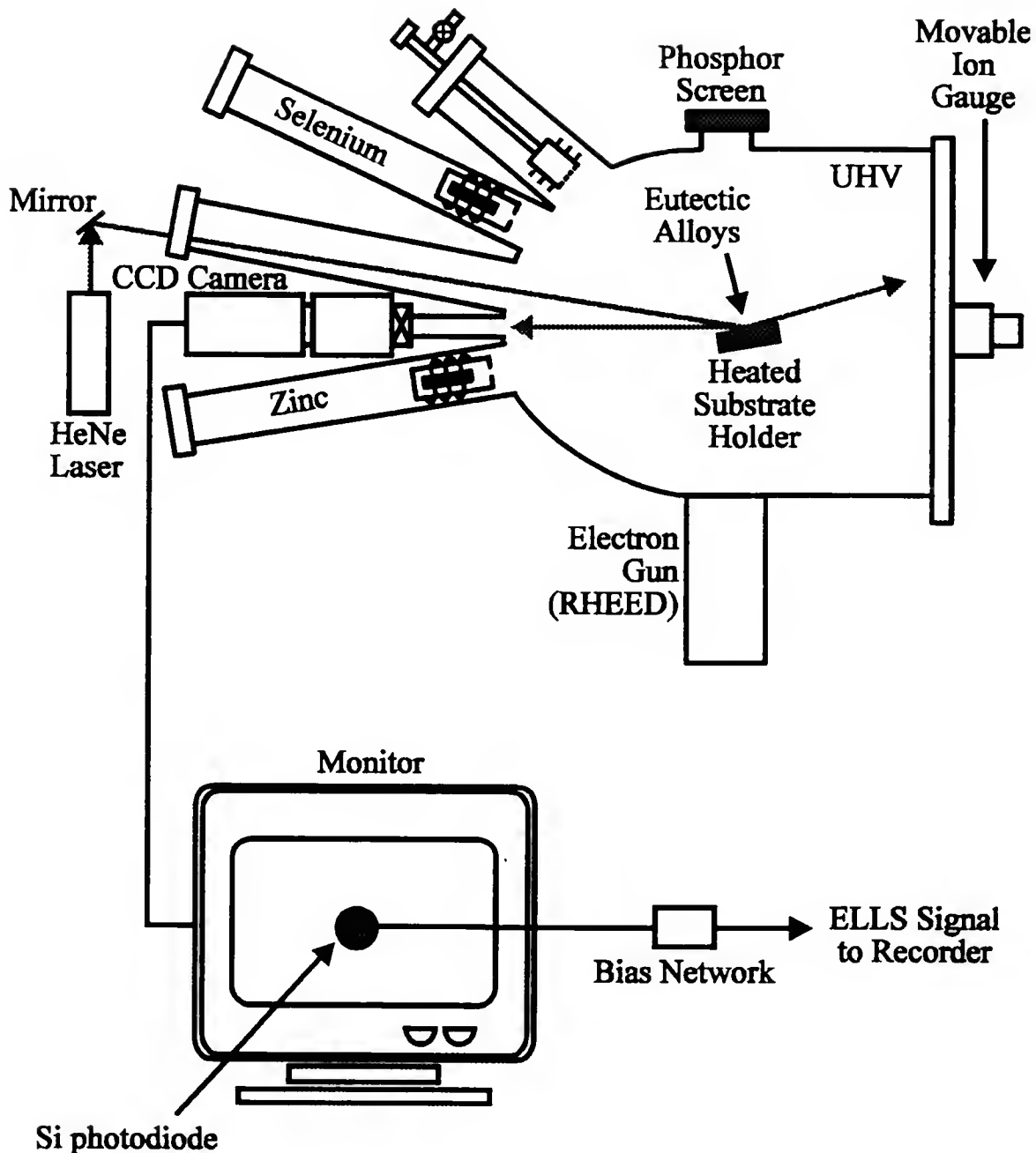


Figure 8 Schematic of the experimental setup used to calibrate precisely the substrate temperature by recording the change in scattered HeNe laser light corresponding to the formation of a eutectic compound from selected binary alloys.

formation. The specular reflection was found to be least sensitive to this event, hence the use of the scattered laser light signal.

Temperature reference standards were formed by electron beam evaporation of selected metals onto appropriate substrates. Specifically, 1000Å of Al was deposited onto Si and 1000Å of Au was deposited onto Ge since the eutectic formation temperatures of these binary alloys are 577 and 356°C, respectively.²⁵ A third reference standard was formed by attaching a piece of In wire to GaAs, which upon reaching 156°C, the melting temperature of In, would wilt over. Prior to being mounted in the MBE growth chamber, all three references were soldered to a single Mo holder with 99.9999% pure In and then immediately transferred to a load-lock mounted on the MBE growth chamber.

The calibration curve shown in Fig. 9 was arrived at by very slowly increasing the T/C temperature from room temperature to 650°C and then ascribing the reference temperatures to events (i.e., wilting of the In wire, Au/Ge eutectic formation, Al/Si eutectic formation) as they occurred. As indicated in the inset of Fig. 9, the error (normalized with respect to the T/C temperature) ranges from approximately -8% near 150°C to approximately -3% near 600°C with best linearity ($\pm 1\%$) being achieved in the range of

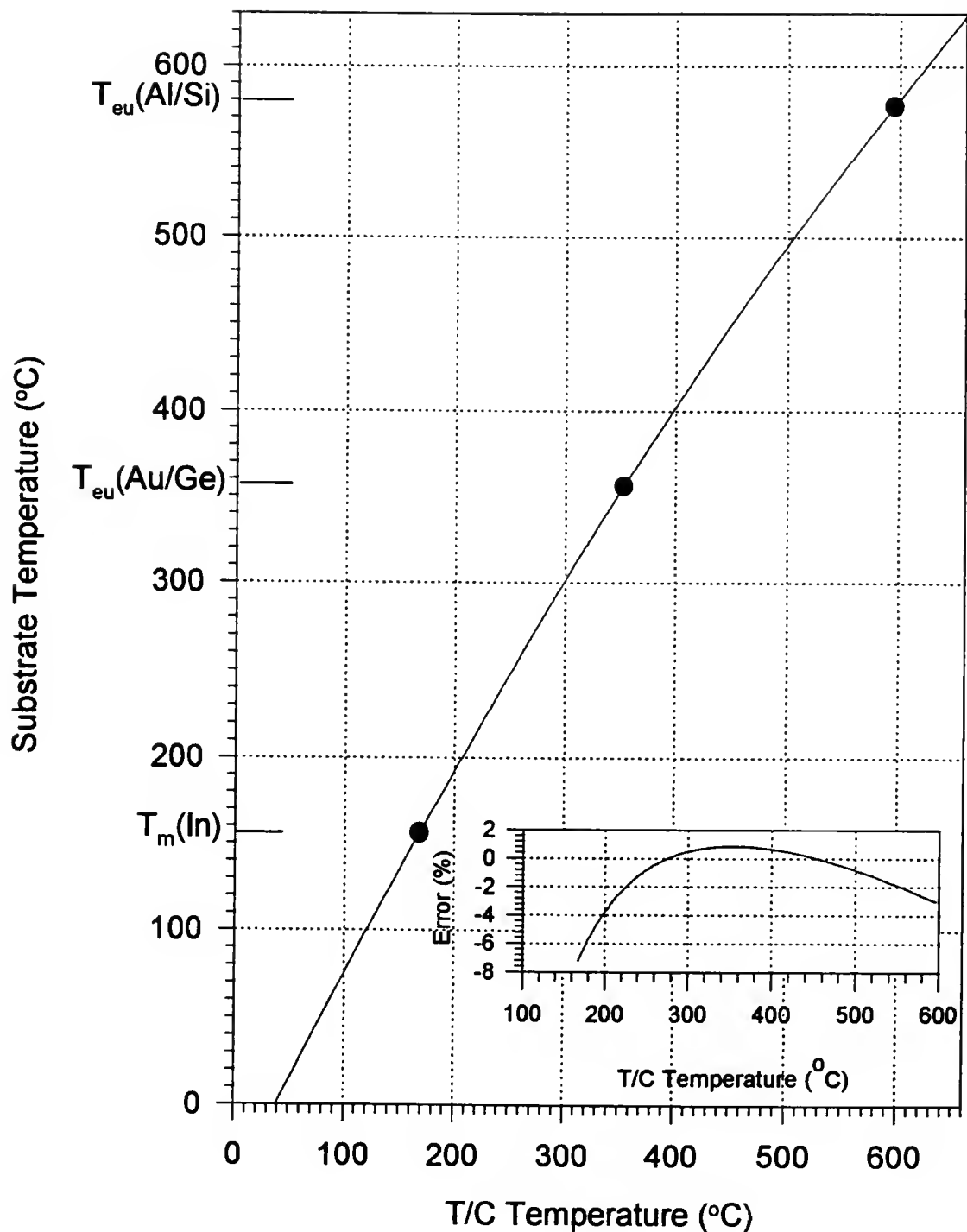


Figure 9 A plot of substrate surface temperature versus thermocouple temperature showing the points associated with eutectic formation. Inset indicates that there was no more than +1/-4% error (normalized to T/C temperature) over the temperature regime explored.

250-500°C. This is a reasonable variation because the emissivity of Mo increases with increasing temperature while its thermal conductivity decreases with increasing temperature. It should be noted that the calibration was used in all future experiments to convert monitored, or T/C, temperature to actual substrate temperature so reported temperatures would be system unspecific allowing the present results to be compared to the literature.

In Situ GaAs Surface Cleaning

The substrates used in the cleaning study were epi-ready, vertical gradient freeze (VGF) grown GaAs(001) oriented 2° towards [110] supplied by American Xtal Technology (Dublin, CA). Prior to being mounted in the MBE growth chamber, the substrates were soldered to a Mo holder with 99.9999% pure In, and then immediately transferred to a load-lock mounted on the MBE growth chamber.

The laser light scattering data recorded from GaAs wafers treated thermally and using a combined thermal/H-atom treatment are compared and contrasted in Fig. 10. A 10°C/minute temperature ramp, which was achieved using a programmable temperature controller, was used to sweep the

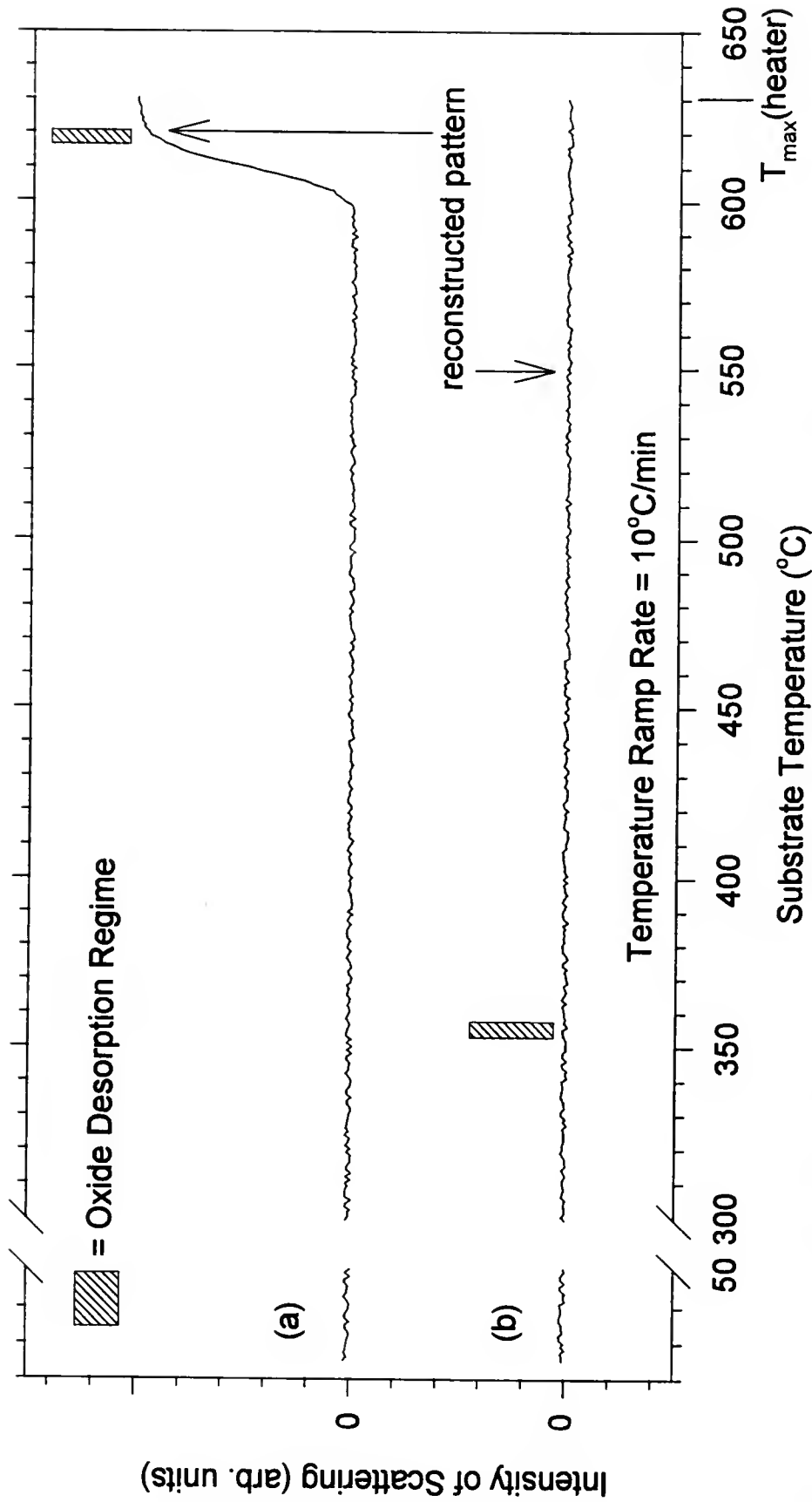


Figure 10 A plot of the intensity of laser light scattering versus substrate temperature (ramp rate = $10^{\circ}\text{C}/\text{min}$). The data was recorded during conventional thermal treatment and during a combined thermal/H-atom treatment of (001)GaAs wafers, (a) and (b), respectively.

temperature from room temperature to the maximum operating temperature (630°C) of the heater station as shown in the figure.

As indicated in Fig. 10(a), conventional thermal treatment of GaAs resulted in an associated surface roughening upon oxide desorption, the oxide desorption process being observed by simultaneous monitoring of the RHEED pattern. This result is in agreement with the observations of Lavoie et al.⁵ In contrast, however, surface roughening did not accompany the oxide desorption process in the case of the combined thermal/H-atom treatment as evidenced by the lack of laser scattering in the oxide desorption regime indicated in Fig. 10(b). Also, the oxide desorption temperature is significantly lower in the case of the combined thermal/H-atom treatment than in the case of conventional thermal treatment, 350-360°C versus 610-620°C, respectively. Similar oxide desorption temperatures have been reported in the literature whenever activated hydrogen has been employed to clean GaAs.^{15-17,19-21} In all cases, the reduction in temperature has been attributed to the fact that the oxygen in the mixed As/Ga oxide (As₂O₃ and Ga₂O₃) readily reacts with hydrogen at reduced temperatures, more so in the case of the arsenic oxide. Specifically, the literature suggests that the arsenic oxide is readily reduced near room temperature, leaving the gallium oxide

to be reduced at a very slow rate, which can be greatly increased by heating the substrate during processing. As can be seen from Fig. 10(b), surface roughening was not observed using the combined thermal/H-atom treatment; apparently such an observation would require operation of the substrate heater beyond its maximum rated power level.

As indicated above, simultaneous monitoring of the RHEED pattern during each treatment indicated when the oxide desorption process was completed. Upon completion of the oxide desorption process, representative RHEED patterns of the atomically clean GaAs surfaces were recorded, and these patterns are shown in Fig. 11. As indicated in Fig. 11(a), the pattern resulting from conventional thermal treatment of GaAs is characteristic of a reconstructed surface, a result that is not surprising because of the presence of dangling bonds at the free-surface upon oxide desorption. In contrast, the RHEED pattern shown in Fig. 11(b), which was recorded from a surface that experienced the thermal/H-atom treatment, is indicative of an unreconstructed surface, a surface where the atoms maintain their bulk-like positions. By removing the H-atom flux and raising the temperature to 550°C, however, the surface reconstructed, as indicated by the RHEED pattern shown in Fig. 11(c), which suggests the presence of dangling bonds as in the case of

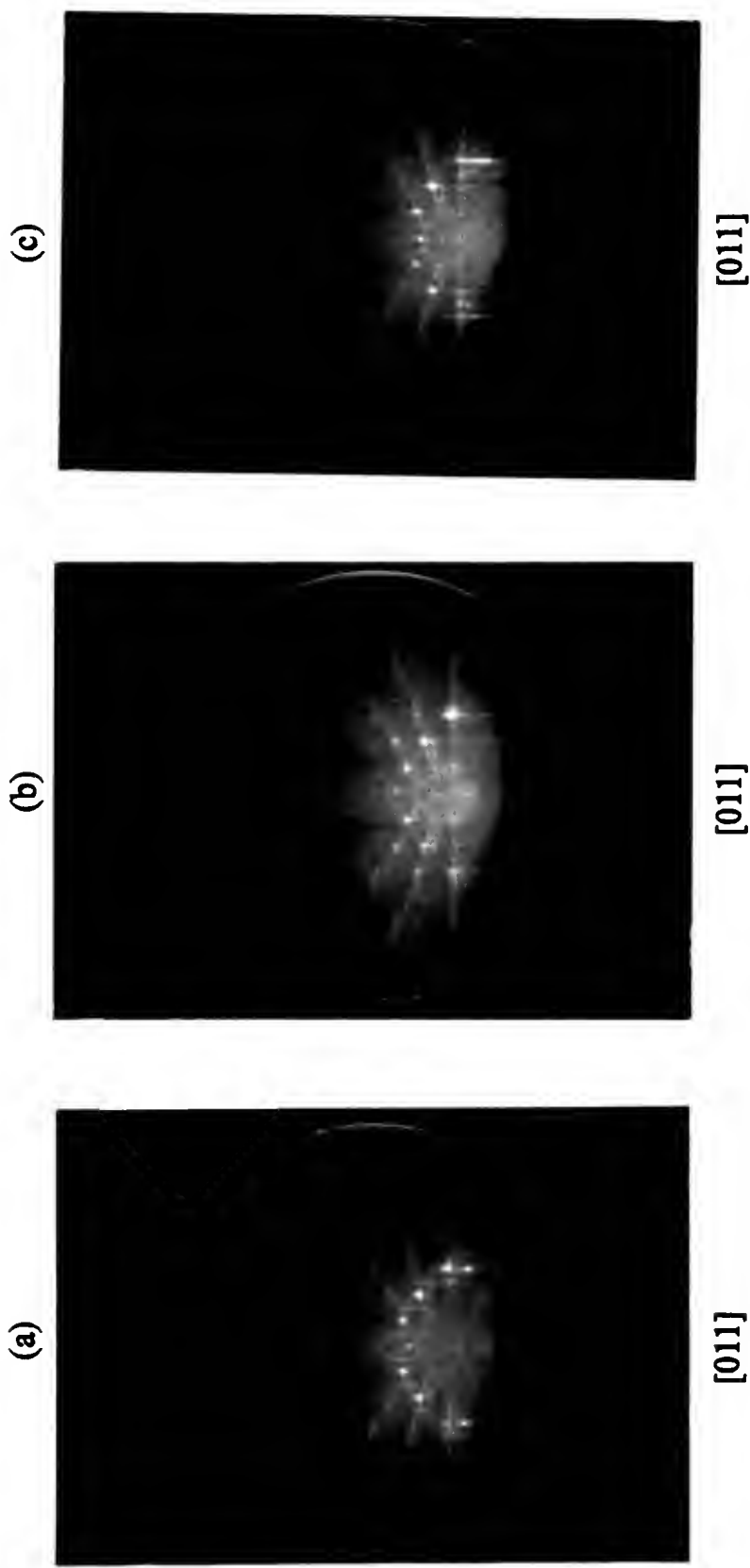


Figure 11 Representative reflection high energy electron diffraction patterns recorded from atomically clean GaAs surfaces resulting from conventional thermal treatment and the combined thermal/H-atom treatment and after removal of the H-atom flux, (a), (b), and (c), respectively.

thermally cleaned surfaces. It is interesting to note that upon lowering the temperature to 150°C and reapplying the H-atom flux, the reconstruction reversed, as indicated by a RHEED pattern that returned to that of Fig. 11(b), suggesting that the H atoms were terminating the dangling bonds. A reconstructed surface was again achieved by removing the H-atom flux and raising the temperature to 550°C, which suggests that the termination effect is reversible. Finally, exposure to unexcited hydrogen gas (H₂) had no effect on the surface reconstruction, which clearly illustrates the enhanced reaction between atomic H and the GaAs surface. These observations (i.e., the effectiveness of H, reconstruction reversibility, and ineffectiveness of H₂) are in agreement with those of O'Keeffe et al.²⁶ and it would seem that the impinging hydrogen atoms terminate the dangling bonds, thus allowing the surface atoms to maintain their bulk-like positions. Although not specifically determined in this case, it can be speculated that the GaAs surface is As-rich following oxide desorption during H treatment because of the similitude between the present results and those of O'Keeffe et al.²⁶ Specifically, they were able to compare a deliberately As-stabilized GaAs surface obtained at high temperature (~700°C) to one obtained at low temperature (~100°C) and they confirmed that a two-folded structure (As-stable 2 X 4 pattern) at high

temperature corresponded to a two-folded structure (As-stable 2 X 1 pattern) at low temperature. Therefore, they concluded that the reconstructed GaAs surface following H treatment must be an As-stable 2 X 1 surface because of the similarity they observed between RHEED patterns. It then follows, based on this final conclusion, that the GaAs surface prior to reconstruction (during H treatment) must necessarily be As-rich. It should be noted that the ZnSe epilayers considered in the following chapter were grown on unreconstructed GaAs surfaces (i.e., GaAs surfaces immediately following H treatment).

Conclusions

GaAs surfaces can be readily cleaned at temperatures at or below 350°C prior to MBE growth when prepared *in situ* using our combined thermal/H-atom treatment, the H-atom flux being derived from a UHV compatible rf plasma source, as opposed to the conventional thermal treatment, which requires temperatures in the vicinity of 600°C. A further benefit associated with the H atom treatment is that the atomically clean GaAs surfaces are specular, making them more suitable for epitaxial growth

than conventional thermally treated GaAs surfaces, which are considerably rougher, as evidenced by laser light scattering observations.

CHAPTER 3

LASER LIGHT SCATTERING DURING ZnSe/GaAs HETEROEPITAXY

Background

Following breakthroughs in the ZnSe p-type doping area^{24,27} emphasis has shifted recently in the wide-bandgap II-VI semiconductor research field toward the provision of lattice-matched widegap II-VI/GaAs epitaxial structures for blue/green diode laser application.²⁸ Although the first blue/green diode lasers represented a considerable achievement^{29,30} the structures employed in the fabrication of these devices were not completely lattice-matched and, consequently, devices exhibited short lifetimes even at reduced temperatures.

It is generally accepted that perfect lattice-matching between widegap II-VI epitaxial materials and GaAs substrates will be a primary requirement with regard to the development of long-lived (at room temperature) ZnSe-based blue/green diode lasers. At present, however, time consuming *ex situ* characterization techniques such as high resolution x-ray diffraction and

cross-sectional transmission electron microscopy are applied to determine the extent of lattice-matching in widegap II-VI/GaAs heterostructures.

The primary objectives of this portion of the work were to develop an *in situ* optical probe which could be used to study the strain relief process associated with mismatched epitaxy in real-time during growth and to attempt through theoretical and experimental approaches to correlate optical information obtained *in situ* with major structural defects associated with plastic deformation.

Experimental Apparatus

MBE Growth Chamber

As in chapter 2, the experiments were carried out in a custom-designed molecular beam epitaxy system equipped with conventional effusion sources for Zn, Se, and Te, a reflection high energy electron diffraction system for assessing substrate surface quality and subsequent epilayer quality, and an ultra-high vacuum compatible rf plasma source which was used to remove the GaAs oxide prior to epitaxy. In addition to these conventional components, the molecular beam epitaxy chamber was also configured with a laser probe apparatus as illustrated in Fig. 12.

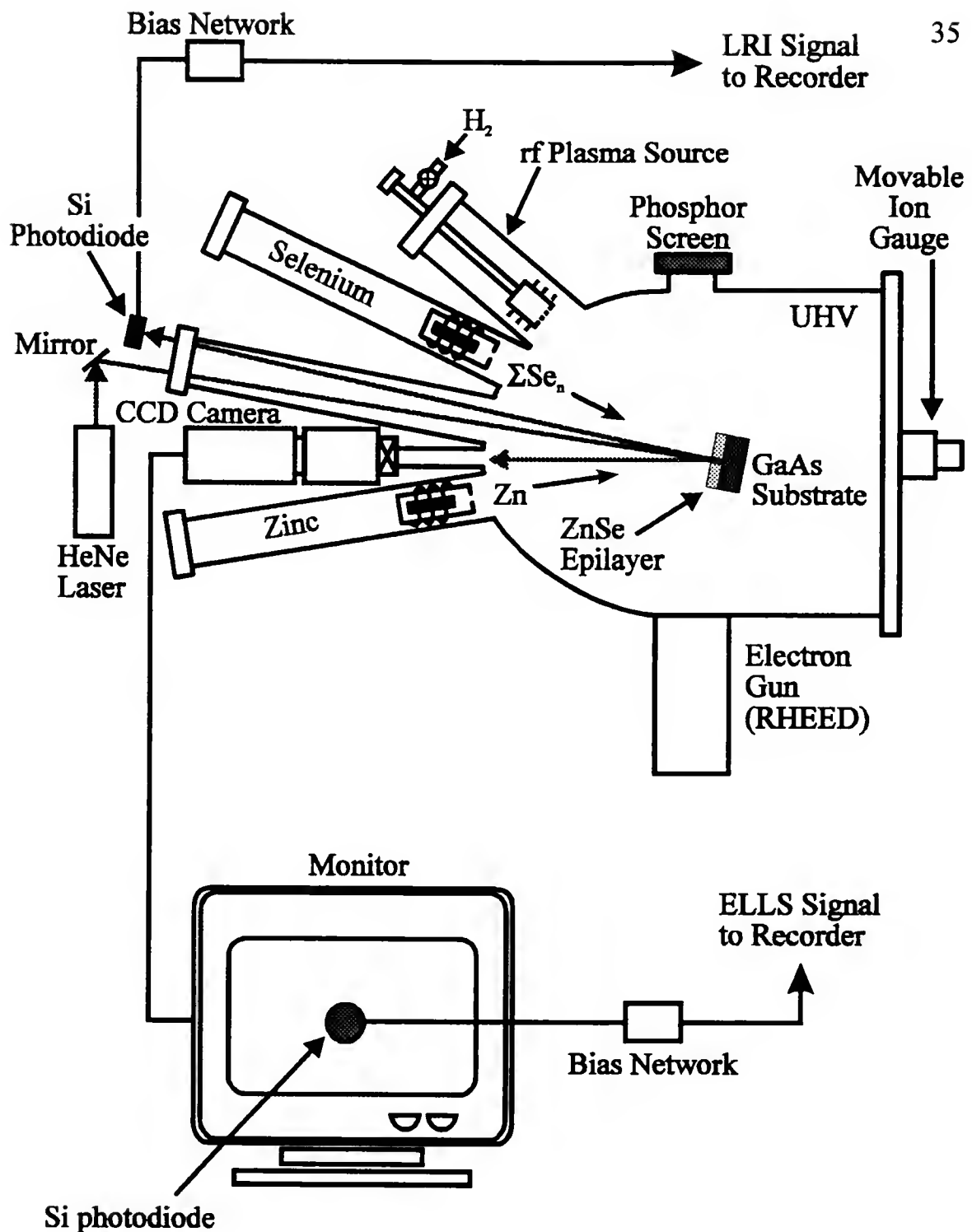


Figure 12 Schematic of the experimental setup used to record elastically scattered laser light (ELLS) and specularly reflected laser light during the molecular beam epitaxial growth of widegap II-VI/GaAs heterostructures.

Laser Probe Apparatus

The apparatus (slightly different than that of chapter 2) consisted of a 1mW HeNe laser ($\lambda=632.8\text{nm}$) mounted outside the MBE growth chamber, the laser beam being directed through a viewport towards the substrate which was mounted on a heated Mo substrate holder. The detector/amplifier stage of the apparatus consisted of a color CCD camera and a video monitor. The camera was mounted outside the system on its own viewport, its optical axis lying 10° away from the optical axis of the incident laser beam, the laser beam having near-normal incidence. The camera was focused on the substrate surface and the visible spot arising from ELLS due to defect evolution was displayed on the video monitor. The intensity of the scattered laser light was quantified by attaching a Si photodiode to the monitor's CRT over the image of the spot and the output voltage from its respective bias network was recorded as a function of time.

The specularly reflected beam was utilized in this experiment to monitor film thickness *in situ* by employing laser reflection interferometry (LRI).⁴ As can be seen from the figure, the HeNe laser was employed to provide a near-normal incident beam at the sample during MBE growth and a silicon wide-area photodiode was used to detect the reflected signal. The

intensity of the reflected signal varied sinusoidally with time during growth due to interference between the reflection occurring at the growing ZnSe free surface and the reflection occurring at the ZnSe/GaAs heterointerface. *Ex situ* film thickness measurements performed on calibration samples using cross-sectional scanning electron microscopy (XSEM) revealed actual film thicknesses which allowed a correlation to be made between oscillation period and film thickness. Specifically, an oscillation period was determined to correspond to ~120nm of deposited material. This oscillation period/film thickness calibration was used to deduce the thickness of the ZnSe/GaAs films in real-time during deposition. It should be noted that the intensities of both the scattered laser light and the specularly reflected laser light were recorded simultaneously so that signal phasing could be compared.

Heteroepitaxy

Particle Contamination Considerations

It was very important that prior to heteroepitaxy, the wafer surface remain smooth and specular such that any subsequent scattering could be attributed to epitaxy and not to pregrowth, *ex vacuo* wafer processing. In chapter 2, it was determined that thermally assisted hydrogen cleaning

promoted such a condition. This condition, however, was only guaranteed provided the wafer enter the MBE chamber in a smooth and specular state (i.e., free of surface defects, particulate matter, etc.).

In an effort to characterize the state of the wafer surface prior to transfer into the load-lock, a full 2" diameter as-received wafer was scanned with a HeNe laser and it was found that scattering could not be detected. Upon cleaving (a practice generally used to economize material), however, the state of the surface was dramatically altered.

As indicated in Fig. 13(a), a number of particles were generated in the vicinity of the cleave line, their number density being $\sim 1700\text{cm}^{-2}$. In an effort to remove the particulate matter, a short burst of compressed chlorodifluoromethane gas from a non-residue dust remover (ultra-filtered to $<0.2\mu\text{m}$) was directed at the wafer surface which reduced the particle count to $\sim 1100\text{cm}^{-2}$, a reduction of $\sim 35\%$ (see Fig. 13(b)). As shown in Fig. 13(c), further exposure to the gas stream (~ 5 seconds) had a detrimental effect as evidenced by a substantial increase in particle density, ~ 10600 to $\sim 35800\text{cm}^{-2}$ depending on the count location. The most probable explanation for the increased particle count is airborne particles being drawn into the low pressure zone surrounding the flowing gas stream and then entering the

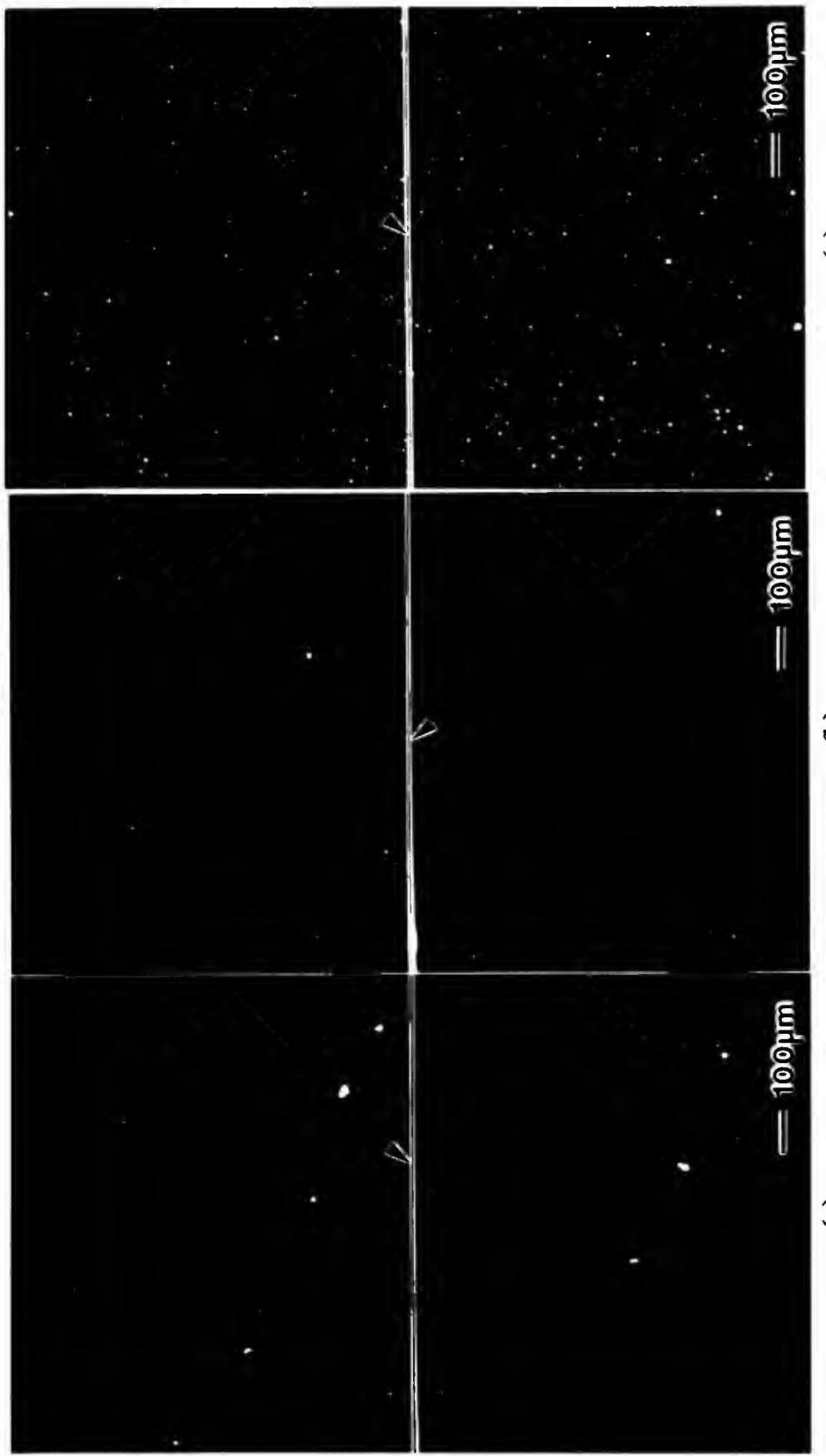


Figure 13 Dark-field optical micrographs showing typical particle densities resulting from cleaving, gas burst cleaning and continuous (~5 seconds) gas flow cleaning, (a), (b), and (c), respectively. Note: the cleave line runs horizontally through the micrographs.

stream to be accelerated towards the wafer by the impinging gas molecules. Electrostatic forces then bind the particles to the wafer surface making them very difficult to remove. Based on this study, it was decided that full 2" diameter as-received wafers would be used for the heteroepitaxy study to ensure that scattering could be attributed to heteroepitaxy.

Ex Situ Substrate Preparation

Two types of substrates were used in the heteroepitaxy study. The first type was epi-ready, vertical gradient freeze (VGF) grown GaAs(001) oriented 2° towards [110] whereas the second type was liquid encapsulated Czochralski (LEC) grown GaAs(001) also oriented 2° towards [110]; their respective manufacturers were American Xtal Technology (AXT) of Dublin, CA and Sumitomo Electric of Hyogo, Japan. Prior to being soldered to a Mo holder with 99.9999% pure In, the Sumitomo wafers were first cleaned and oxidized by placing them in an ultra-violet (UV) ozone cleaning system manufactured by UVOCs Incorporated for 6 minutes. The combination of UV ($\lambda=254$ and 185nm) radiation and ozone generated by these systems have been shown to cause rapid oxidation and removal of trace organic residues.³¹ Furthermore, oxides formed from ozone exposure provide a more controlled

alternative to thermal and air formed oxides.³² The AXT wafers, however, were untreated as they were epi-ready and required no pre-cleaning before being soldered to the Mo holder. As a result, neither substrate material underwent any wet chemical processing and following In mounting, they were immediately transferred to a load-lock mounted on the MBE growth chamber.

Laser Light Scattering from Typical Epilayers

As illustrated in Fig. 14, in the case of heteroepitaxy on the AXT wafers, laser light scattering was not detectable (by the detection system) upon ZnSe growth initiation until approximately 390nm of material had been deposited whereupon increasingly intense scattering was detected with increasing film thickness. The waveform also had an oscillatory form as shown in the figure. It should be noted that in order not to observe scattering upon growth initiation, it was imperative that the GaAs surface be specular following oxide removal as discussed in chapter 2. The growth was terminated near 840nm to avoid saturating the detection system as discussed in chapter 2. With the exception of a detectable onset of scattering at approximately 280nm, a similar waveform was obtained for the case of

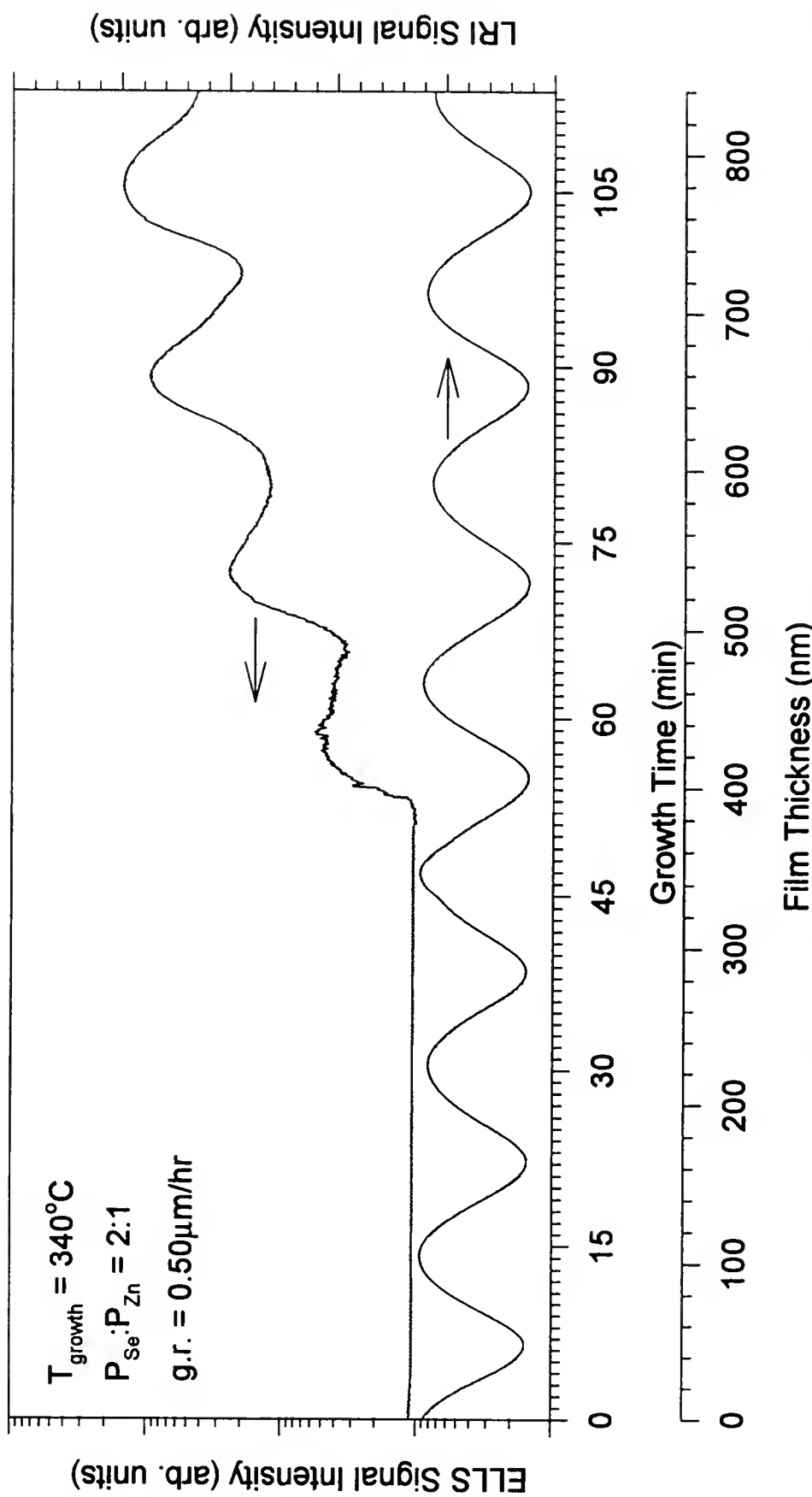


Figure 14 Intensity of laser light scattering occurring near the ZnSe/GaAs (GaAs supplied by American Xtal Technology) heterointerface as a function of ZnSe epitaxial deposition time and layer thickness. Also included in the figure is a laser reflection interferogram to compare phasing.

heteroepitaxy on the Sumitomo wafers as indicated in Fig. 15. Observation of the RHEED pattern following deposition in each case indicated a smooth ZnSe free-surface which suggested that the source of the observed laser scattering was at a location other than the free-surface.

The most striking feature of Figs. 14 and 15 is the π phase difference between the ELLS signal and the LRI signal which, using optical ray tracing, can be explained by placing an emitter at the heterointerface and considering intense scattering at the heterointerface as opposed to the free surface. To explain further, the qualitative model illustrated in Fig. 16 was developed.

As indicated in Fig. 16, the laser beam impinges on the sample at near-normal incidence and a portion of the beam is transmitted into the epilayer and proceeds towards the heterointerface. It is considered, that in addition to specular reflection off the heterointerface, a small portion of the beam is scattered into other (nonspecular) angles due to the presence of defects which occur during epitaxy. For simplicity, only that angle which points in the direction of the detection system as indicated in the figure is considered. The scattered beam traverses the epilayer and in addition to transmission through the free surface, a portion of the beam is redirected back towards the heterointerface by reflection off the epilayer side of the

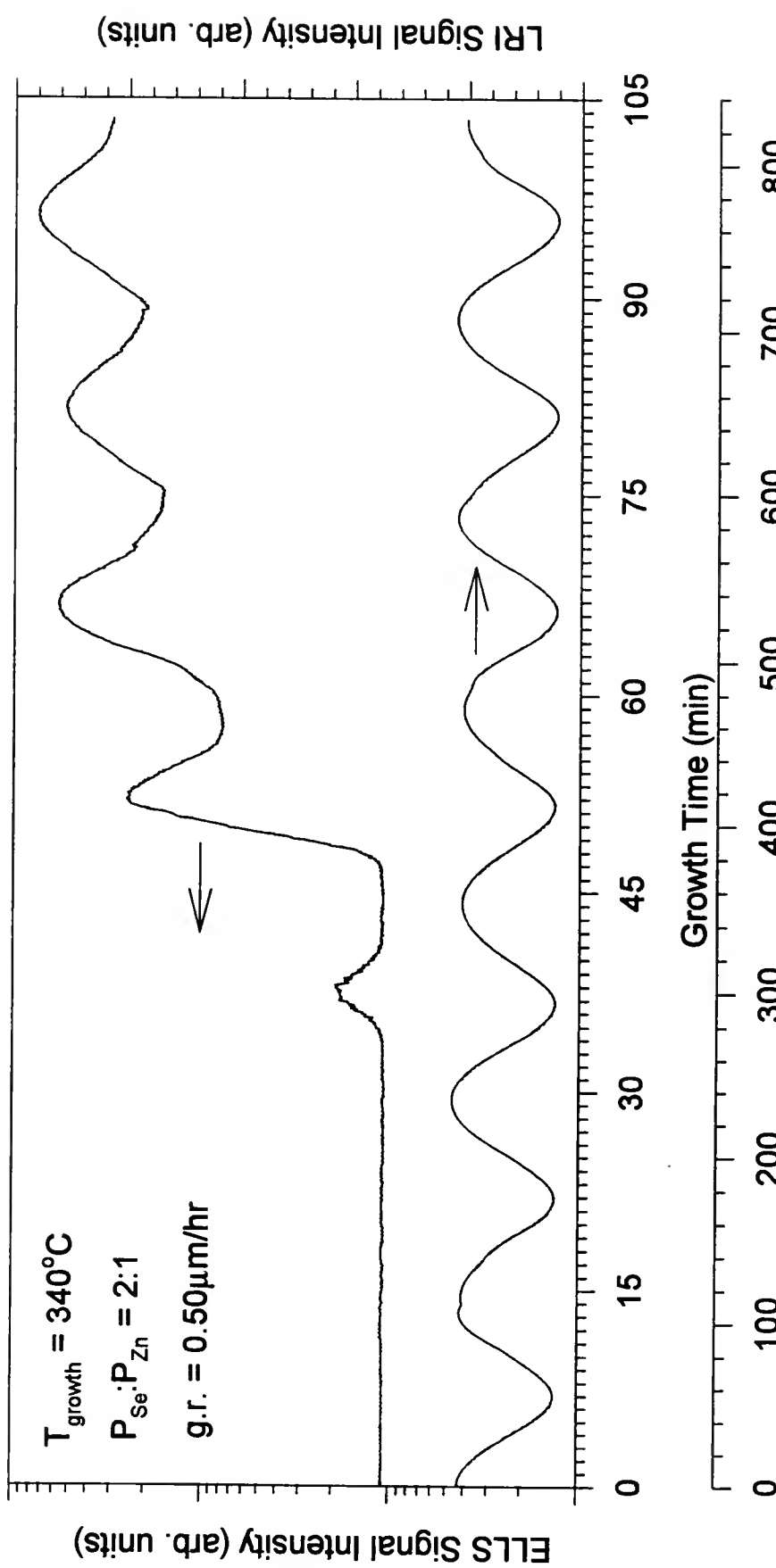


Figure 15 Intensity of laser light scattering occurring near the ZnSe/GaAs (GaAs supplied by Sumitomo Electric) heterointerface as a function of ZnSe epitaxial deposition time and layer thickness. Also included in the figure is a laser reflection interferogram to compare phasing.

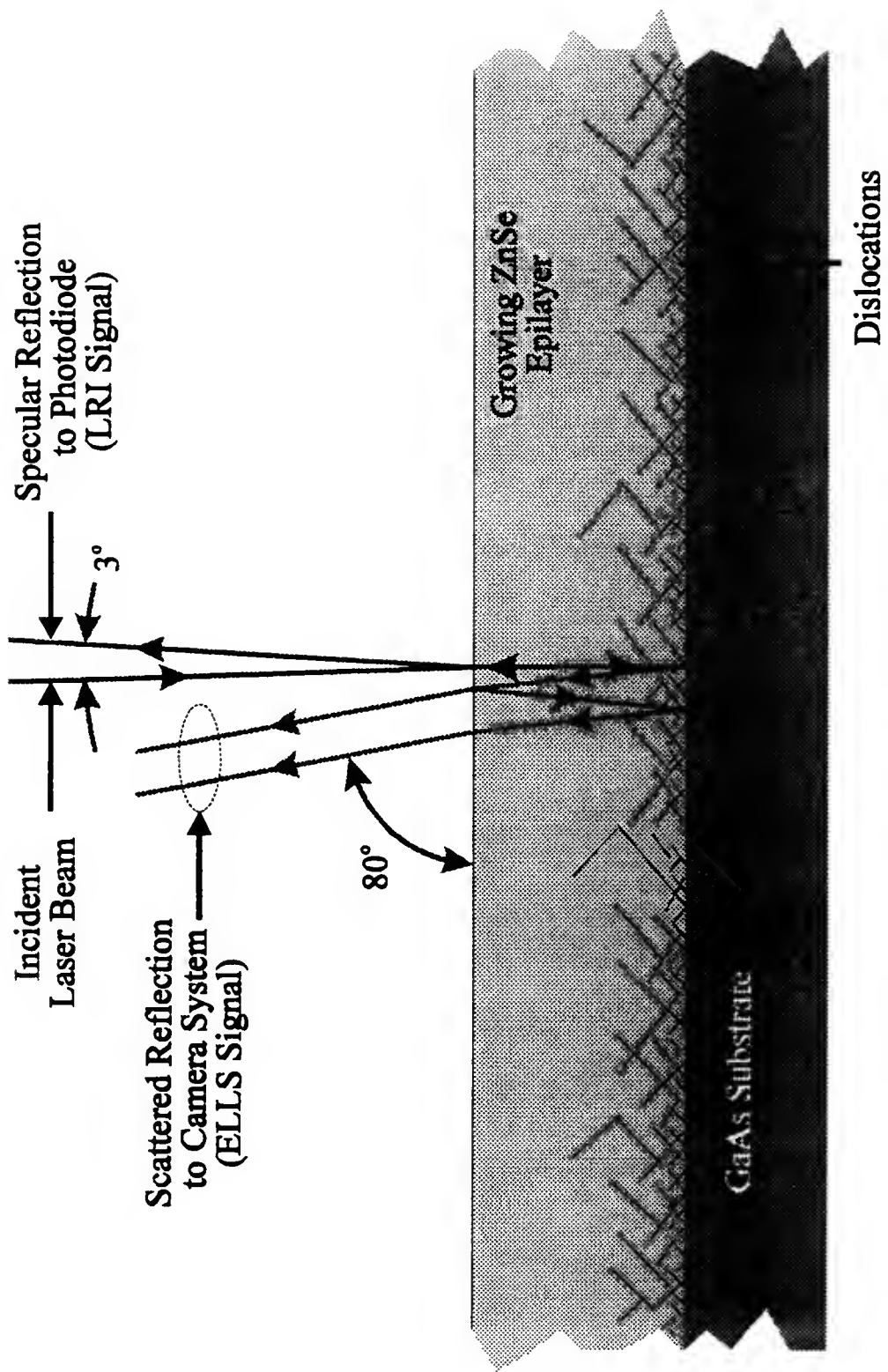


Figure 16 A ray model illustrating the employment of a HeNe laser beam to probe the ZnSe/GaAs heterointerface during epitaxial deposition. Defect evolution gives rise to a scattered signal which was detected and quantified using the apparatus shown in Fig. 12.

free-surface. Since the index step from epilayer to vacuum is negative, no phase shift is introduced upon reflection. The reflected portion of the beam again traverses the epilayer, reflects off the heterointerface, and then makes a final pass through the epilayer to emerge on the vacuum side of the free-surface. At this point, a $\pi+2\delta$ phase shift has been introduced, π resulting from prior reflection off the heterointerface and 2δ resulting from traversing the epilayer twice. The phase difference, Δ_{ELLS} , between the newly emergent beam and the original portion of the scattered beam is then $2\delta + \pi$ which is necessarily a function of the wavelength of the laser, λ , the refractive index of the epilayer, n , the thickness of the epilayer, z , and the angle of transmittance within the epilayer, θ . In a similar manner, it can be easily shown that $\Delta_{\text{LRI}} \approx 2\delta$ since $\theta_{\text{LRI}} \approx \theta_{\text{ELLS}}$ due to the small angles involved. Finally, $\Delta_{\text{ELLS}} - \Delta_{\text{LRI}} = \pi$ and hence the π phase difference between the ELLS signal and the LRI signal as observed in Figs. 14 and 15.

It is interesting to compare the present results with those of Olson and Kibbler³³ who employed a similar technique to monitor scattering from GaP during MOCVD of GaP/Si. The GaP/Si system is very similar to the ZnSe/GaAs system with respect to lattice mismatch (0.36%) and refractive index steps at 632.8nm and therefore it seems reasonable to assume that

under similar conditions, similar results may be achieved. Comparing sets of data, it is apparent that their data resembles the LRI data in Figs. 14 and 15 which would place the source of their scattering outside the epilayer or more appropriately, at the free-surface. They do indeed attribute their ELLS signal to surface scattering and it is quite easy, using corollaries to the arguments above, to show the lack of a π phase difference between a ELLS signal and a LRI signal for such a case.

Laser Light Scattering from Very Thick Epilayers

To experimentally demonstrate the case of surface scattering, a very thick ($>30\mu\text{m}$) ZnSe film was grown on an AXT wafer since we had observed in the past via RHEED observations that the surfaces of very thick ZnSe layers appear to be rather rough. Upon initiating growth, the data resembled that of Fig. 14 in that the ELLS and LRI signal phasing was π . Very much later on, however, the ELLS and LRI signal phasing shifted to, and remained at, 0 as can be observed in Fig. 17. Observation of the RHEED pattern following deposition suggested a rough surface as indicated by a spotty pattern. Upon removing the film from the growth chamber it was observed that it had a cloudy appearance which suggested that the

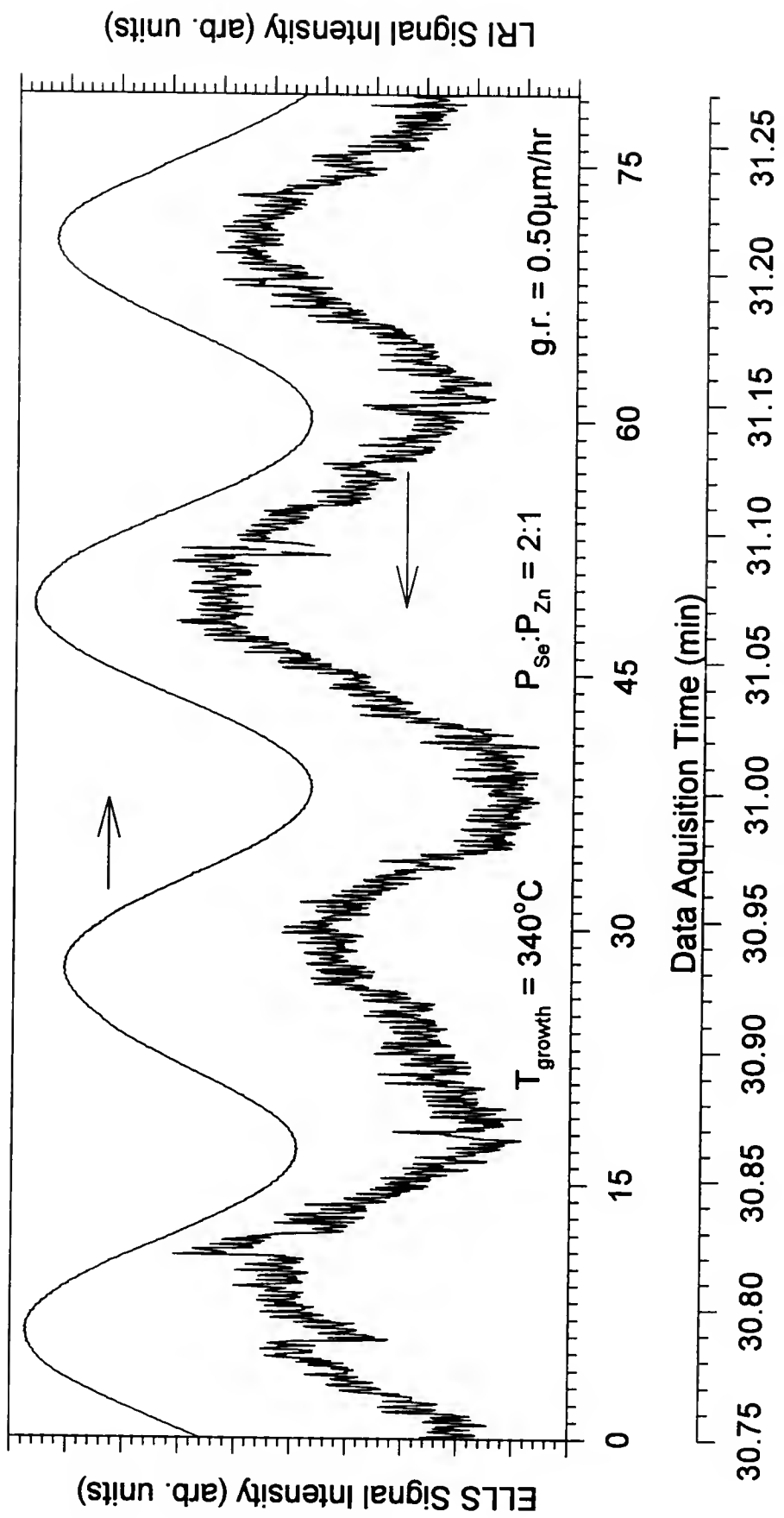


Figure 17 Intensity of scattering occurring near the ZnSe/GaAs (GaAs supplied by Sumitomo Electric) heterointerface as a function of ZnSe epitaxial deposition time and layer thickness for a very thick ($\sim 30 \mu\text{m}$) film. Also included in the figure is a laser reflection interferogram. Note that the signals are in phase for this case.

surface had degraded as expected. Scanning electron microscopy (SEM) was employed to explore the nature of the degradation and the micrographs in Fig. 18 compare and contrast the surfaces of a very thin (60nm) film, a typical film (840nm), and the very thick ($\sim 30\mu\text{m}$) film. It should be noted that all the films presented in Fig. 18 were grown on AXT wafers.

The very thin and typical film, Figs. 18(a) and (b), respectively, were essentially featureless except for some debris which aided in focusing the scanning electron microscope. As suspected, however, the very thick film presented a radical departure from a typical specular surface as evidenced by the presence of a large number of features as shown in Fig. 18(c). As can be observed in the figure, the surface was covered with large faceted features ($\sim 13800\text{cm}^{-2}$) and smaller interspersed features ($\sim 7000\text{cm}^{-2}$) which could possibly serve as seeds for the larger features. These large and small features, because of their size, shape, and distribution, were clearly responsible for the observed scattering and substantiate, to a large extent, the premise that a π phase shift is indicative of heterointerface scattering while a 0 phase shift is indicative of surface scattering. Consequently, the present results clearly differ from previously published results that have concerned surface scattering.

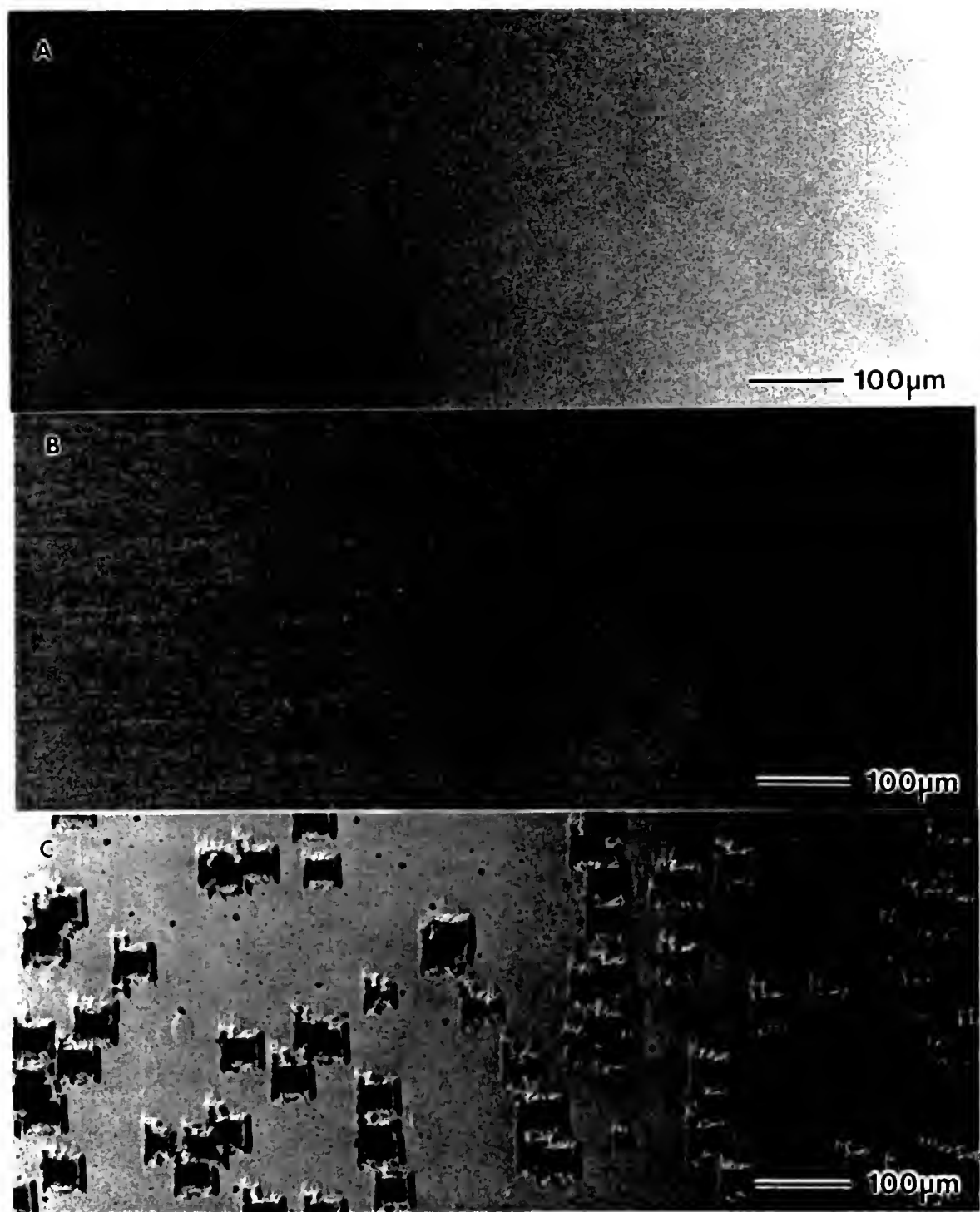


Figure 18 Plan-view scanning electron micrographs (of ZnSe/GaAs) indicating the surface features present on a thin (~60nm), thick (~840nm), and very thick (~30μm) film, (a), (b), and (c), respectively.

Structural Characterization

Many of the characteristics of the optical data presented in Figs. 14 and 15, such as the amplitude of the modulation and the "DC component" of the ELLS signal, are dependent on the optical properties of the heterointerface as well as its morphological properties, these characteristics being controlled by the multiplication and propagation of defects near the heterointerface while the film is growing.

To investigate the defect structure near the heterointerface as a function of film thickness with respect to both the AXT and Sumitomo wafers, two series of 6 epilayers were grown to thicknesses of 60, 120, 300, 360, 600, and 840nm. Plan-view transmission electron micrographs (PTEM) of these epilayers are compared and contrasted in Fig. 19.

As can be observed from Fig. 19, there is a general trend in defect density which mirrors the increase in optical scattering data presented in Fig. 20, a compilation of Figs. 14 and 15. Furthermore, the optical data in Fig. 20 suggests that there was a difference in epilayer quality which was dependent on the type of substrate used. Specifically, the detectable onset of scattering in the case of epilayers grown on AXT wafers was near 400nm (see Fig. 20(a)) while that of epilayers grown on Sumitomo wafers was near

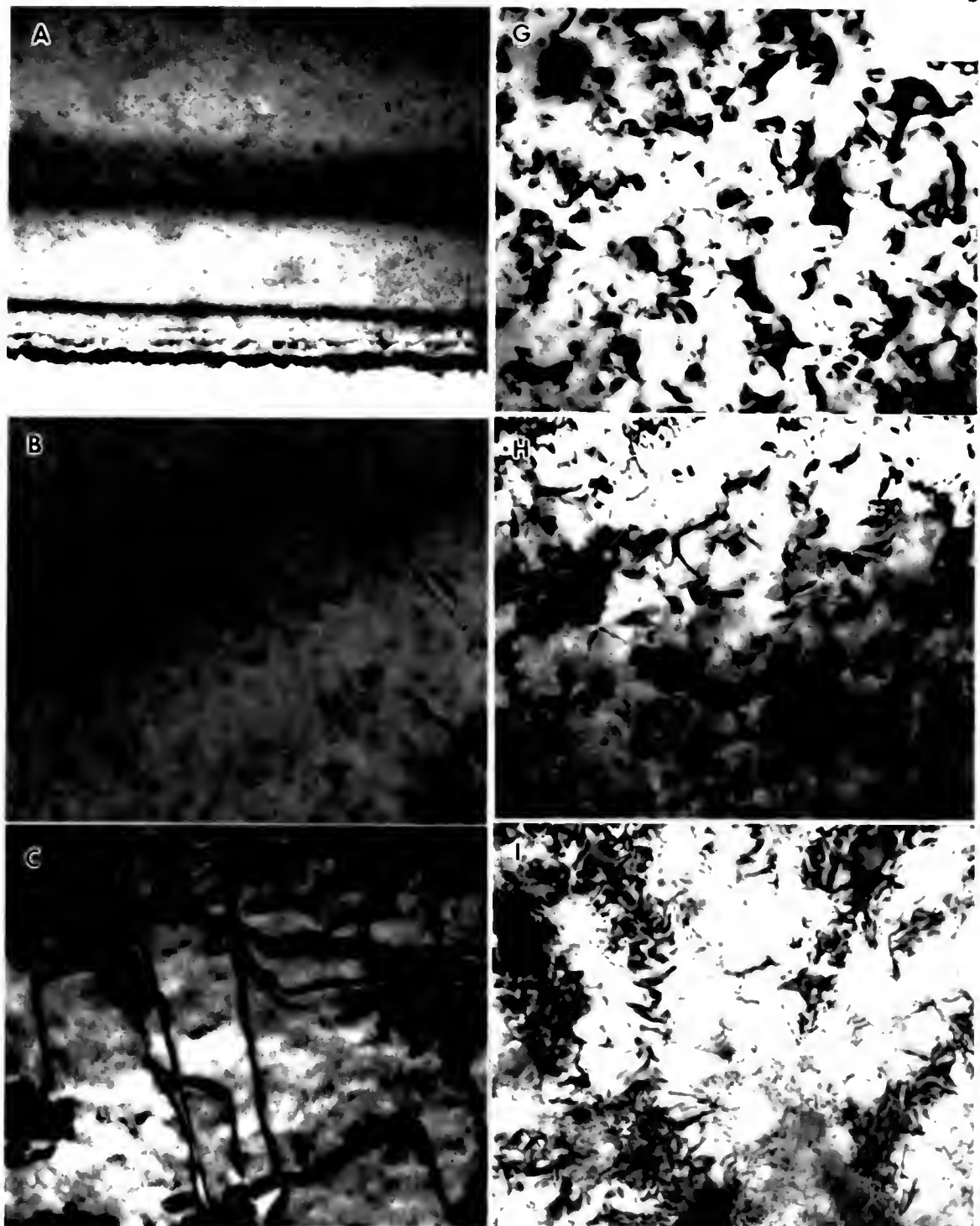


Figure 19 A matrix of plan-view transmission electron micrographs (70,000X) comparing and contrasting the defects present near the ZnSe/GaAs heterointerfaces as a function of film thickness (row 1 through 6 = 60, 120, 300, 360, 600, and 840nm, respectively) and substrate type (column 1 and 2 = American Xtal Technology and Sumitomo Electric, respectively).

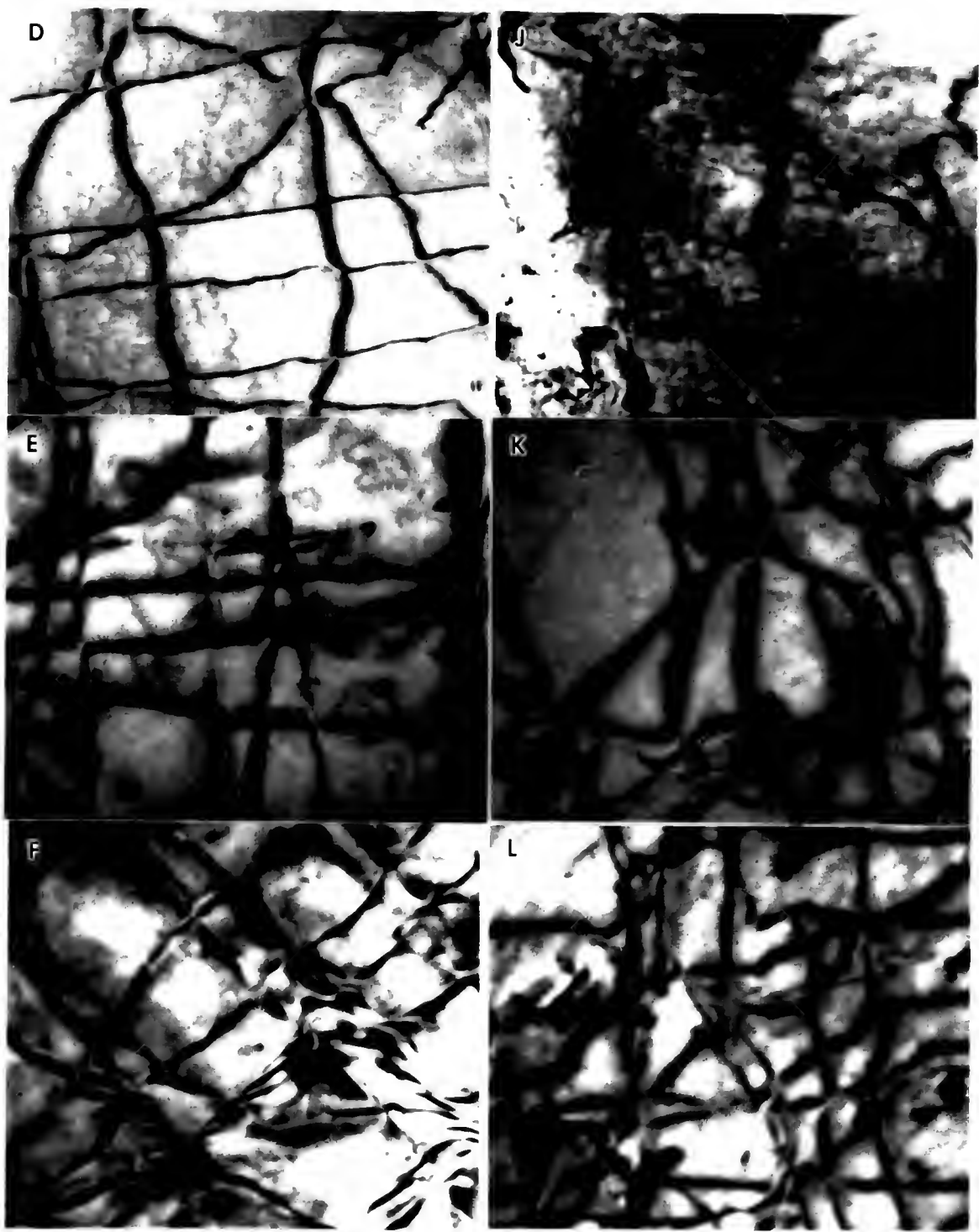


Figure 19 Continued.

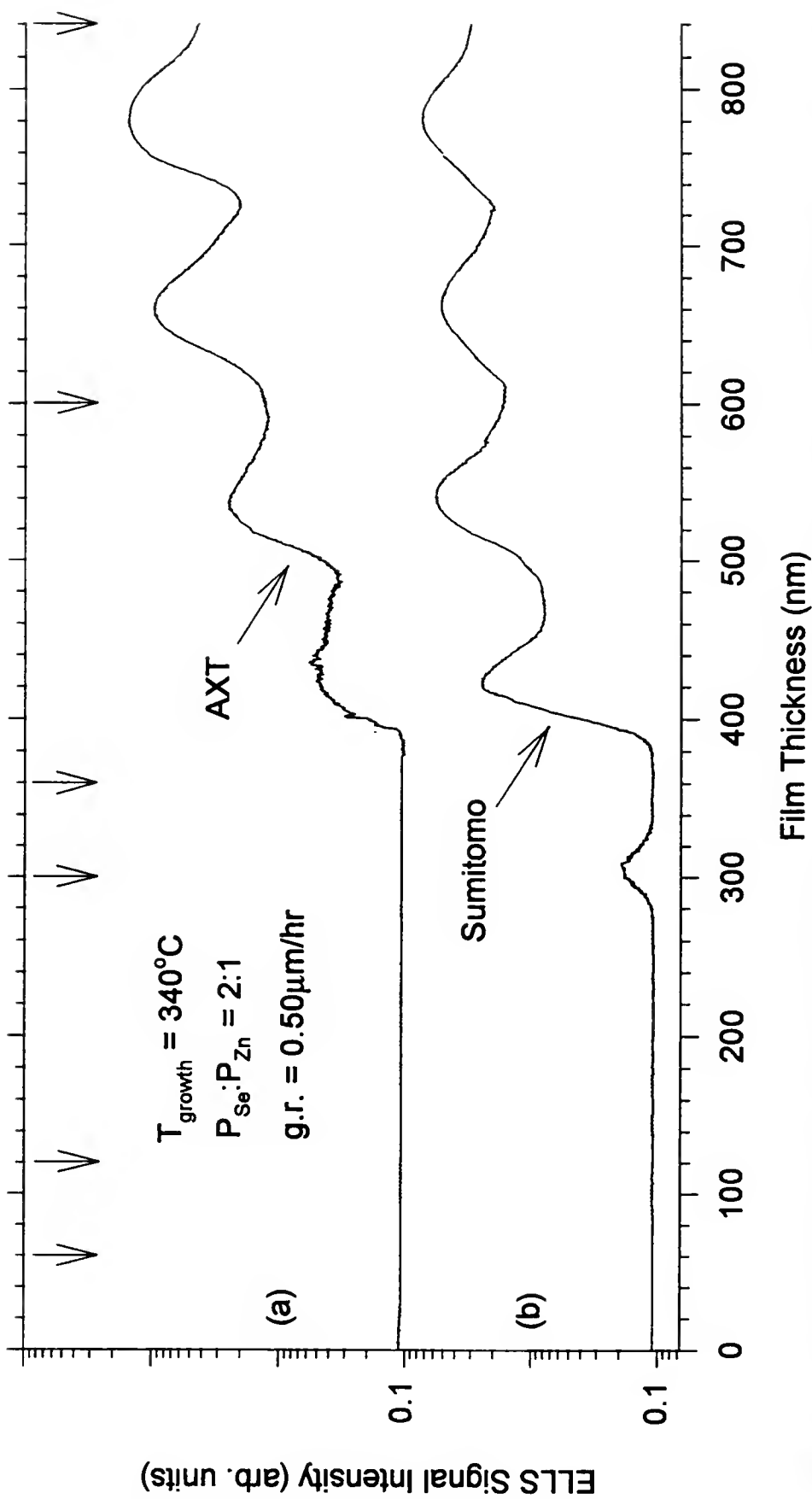


Figure 20 Recompilation of laser scattering data presented in Figs. 14 and 15 which compares and contrasts the laser scattering from an epilayer grown on an American Xtal Technology GaAs wafer to that of an epilayer grown on a Sumitomo Electric GaAs wafer. Epilayers of the thicknesses indicated by the vertical arrows were targeted for structural characterization. Note the difference in the detectable onset (in terms of layer thickness) of scattering.

280nm (see Fig. 20(b)). This difference can most likely be attributed to the different defect structure present near the heterointerface for layer thicknesses ranging from 60 to 300nm (compare Figs. 19(a)-(c) and Figs. 19(g)-(i)). Specifically, the micrographs of epilayers grown on AXT wafers indicate a typical defect evolution from nearly dislocation free material (see Figs. 19(a) and (b)) to dislocated material (see Fig. 19(c)) as a result of exceeding the critical thickness ($\sim 180\text{nm}$)³⁴ for ZnSe/GaAs. Those micrographs associated with epilayers grown on Sumitomo wafers (see Figs. 19(g)-(i)), however, indicate some other defect structure near the heterointerface whose density increased with increasing film thickness to 300nm. High resolution transmission electron microscopy (HRTEM) was performed on these films and despite the presence of these defects, the epilayers remained single crystal and excellent registry was maintained across the ZnSe/GaAs heterointerface. A representative selected area diffraction pattern (SADP) and high resolution cross-sectional transmission electron micrograph (HRXTEM) are shown in Figs. 21(a) and (b), respectively, to corroborate these observations.

Beyond 300nm, the defect structures of the epilayers with respect to substrate type became increasingly similar with respect to defect type and

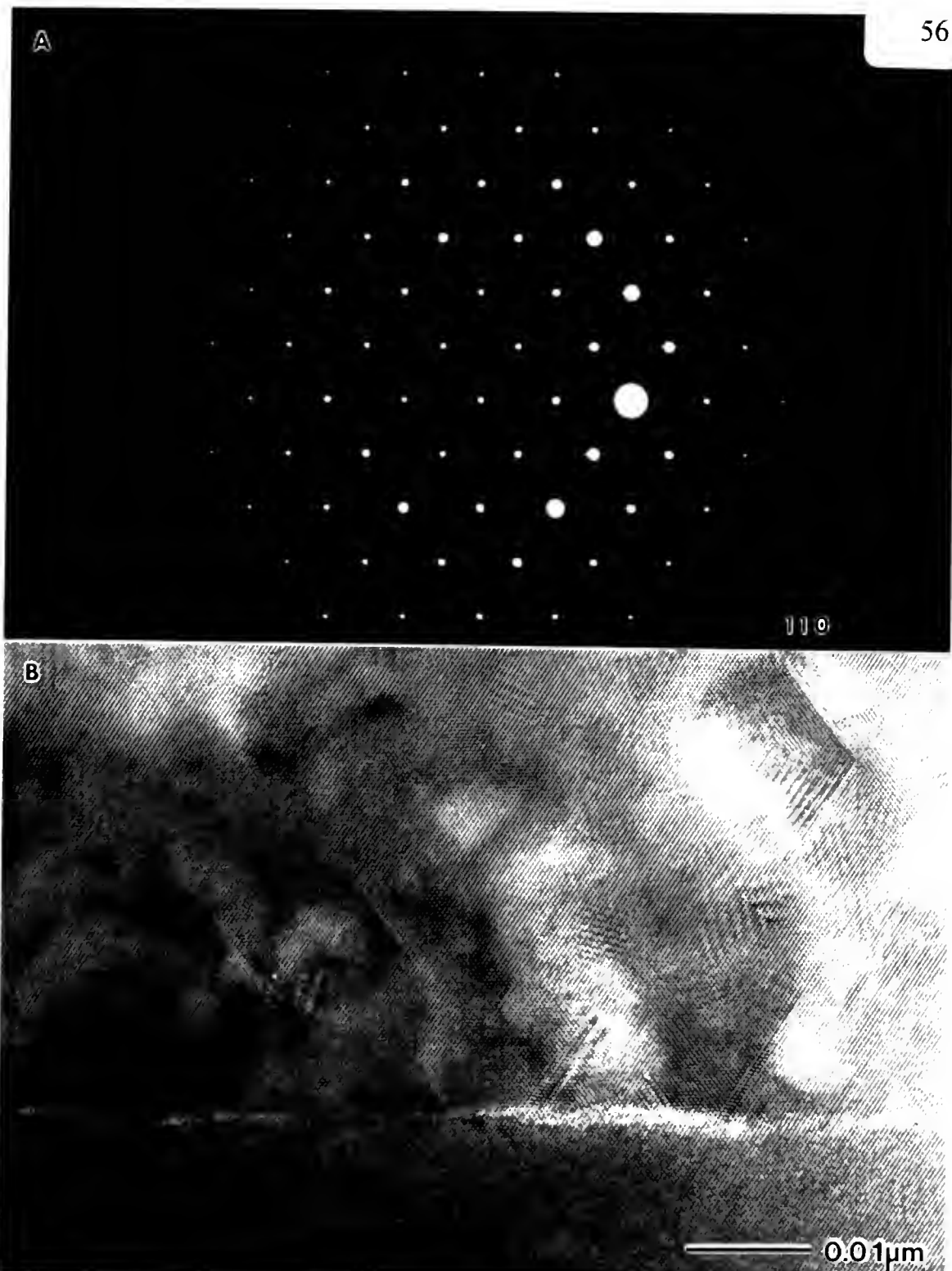


Figure 21 A representative selected area diffraction pattern and high-resolution cross-sectional transmission electron micrograph which are indicative of the crystallinity and defect type present in the epilayers represented by the micrographs shown in Figs. 19(g)-(i).

density which correlates well with the similitude of the optical data following 500nm of film deposition (see Fig. 20).

Lattice Mismatch Sensitivity

The laser probe technique was also applied during the MBE growth of ZnTe/GaAs epilayers in an effort to explore the technique's sensitivity to lattice-mismatch. The scattering data recorded from the ZnTe/GaAs system is compared and contrasted to that observed from the ZnSe/GaAs system in Fig. 22. It should be noted that these epilayers were grown on Sumitomo wafers in an effort to minimize consumption of AXT wafers.

As can be seen from the figure, the detectable onset of scattering from the ZnTe/GaAs material system occurred at ~140nm whereas the detectable onset of scattering from the ZnSe/GaAs material system occurred at ~280nm, much later in terms of layer thickness. Furthermore, the rate of change of scattering (with respect to layer thickness) was greater in the case of ZnTe/GaAs. Both of these observations seem to be highly correlated with the degree of lattice-mismatch as indicated in the figure which would suggest that the optical system is entirely suitable for determining the extent of lattice mismatch.

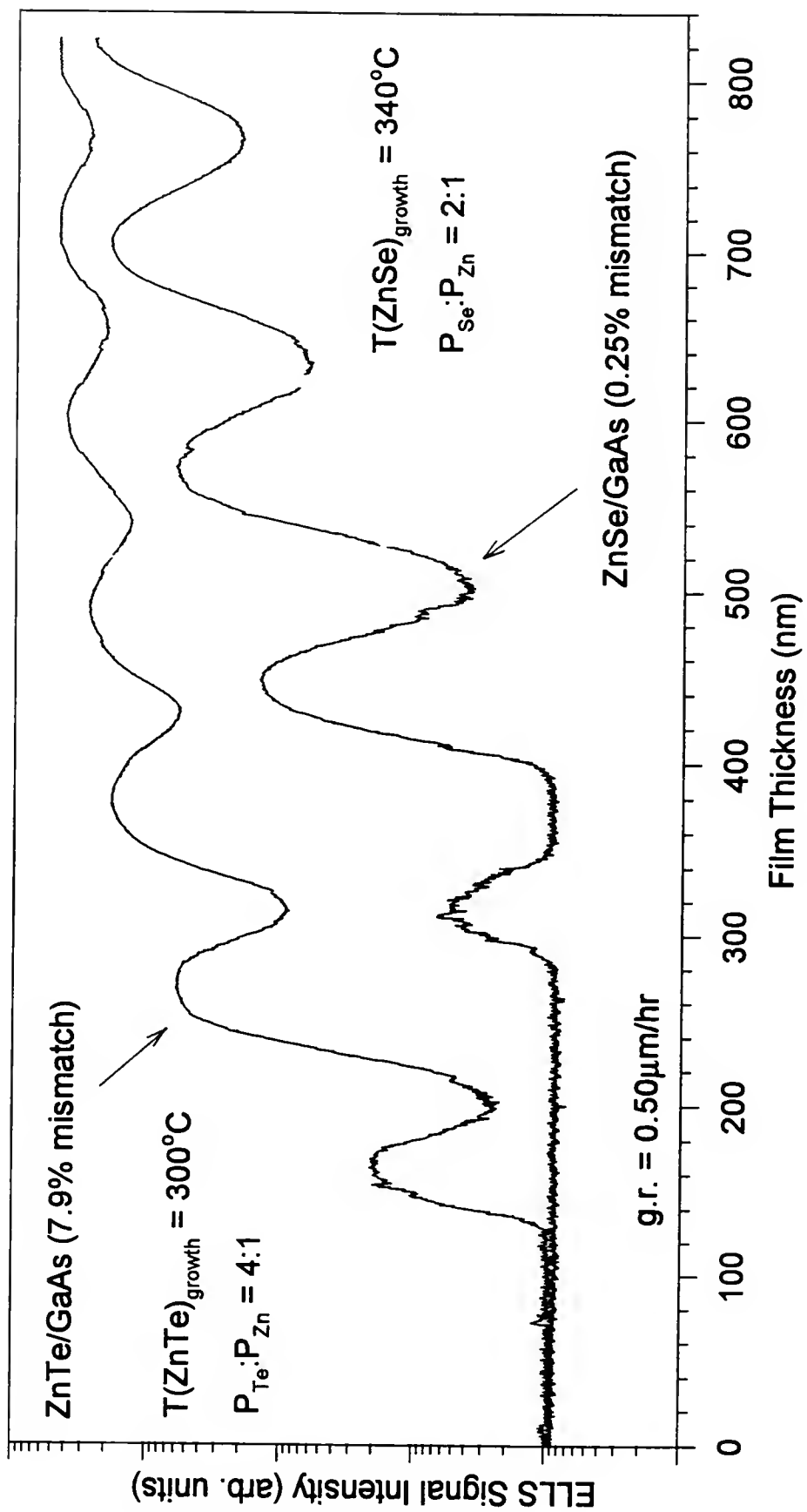


Figure 22 Elastically scattered laser light data recorded in real-time during the deposition of ZnSe/GaAs and ZnTe/GaAs heterostructures. The lattice-mismatches indicated correspond to room temperature lattice-mismatches. Note the difference in detectable onset (in terms of layer thickness) of scattering.

Conclusions

In conclusion, the *in situ* optical probe described above is entirely capable of detecting plastic deformation in lattice-mismatched heteroepitaxial systems, such as ZnSe/GaAs, in real-time during epitaxial deposition. Furthermore, the technique by its real-time nature is appropriate for defect evolution monitoring.

It is further concluded that the observation of a π phase shift between the LRI signal and the ELLS signal is indicative of heterointerface scattering rather than surface scattering in the ZnSe/GaAs heterostructure case.

Finally, should perfectly lattice-matched structures be grown on "ideal" substrates, the laser light scattering reported here should not be detected which could have important consequences for the provision of lattice-matched structures for widegap II-VI/GaAs diode lasers, for instance.

CHAPTER 4 THEORY

The Role of Electric Microfields

A general trend that has been observed is that the band-edge absorption in a semiconductor is shifted to lower energies upon plastic deformation of the crystal, the magnitude of the energy shift being dependent upon the extent of the deformation.³⁵ An interesting explanation which has been proposed to account for the absorption-edge shifting phenomenon concerns the presence of strong electric fields around the resultant dislocations.³⁵ It has been argued, in fact, that the similitude of the absorption behavior in strong electric fields (Franz-Keldysh effect) and following plastic deformation is striking.³⁵ Also, arguments have been made which suggest that in order to present a unified theory of exponential absorption edges in both ionic and covalent materials, electric microfields must be considered.³⁶ Based on the aforementioned evidence the possibility is considered that electric microfields associated with heterointerface defects, arising due to lattice-

mismatch strain relief, are responsible for the observed laser light scattering local to the ZnSe/GaAs heterointerface.

The following discussion pertains to consideration of electric microfields. The field distribution around a dislocation is first considered with regard to three different potentials, namely the deformation potential, the charged dislocation potential, and the piezoelectric potential. Second, the magnitudes of these fields are considered and subsequently the electro-optic effect is evoked in order to argue that a refractive index perturbation sufficient to scatter light could result in the present material system as a consequence of electric microfields.

Deformation Potential

As a result of the strain field surrounding the core of a dislocation line, strong local distortions of the crystal potential occur in the vicinity of the dislocation's core. Farvacque and Lenglart³⁷ originally formulated the Fourier transform of the deformation potential and later Vignaud and Farvacque³⁸ calculated its inverse Fourier transform which results in the deformation electric field as a function of real space as shown in Eq. 1.

$$E_{def}(r) = \frac{ZeNb_c(1-2\nu)}{16\pi^4\epsilon_0\epsilon_L(1-\nu)} \sin(\theta) I(r/\lambda_G) \quad (1)$$

where

$$I(r/\lambda_G) = \int_0^{\infty} \frac{K}{K^2 + (r/\lambda_G)^2} \cos(RK/r) J_1(K) dK \approx \frac{1}{1.03 + 0.283(r/\lambda_G) + 0.7198(r/\lambda_G)}$$

and where r and θ are cylindrical coordinates, Z is the number of valence electrons ($Z=4$ on average for zincblende structures), e is the charge on an electron, N is the number density of atoms, b_c is the edge component of the Burgers vector, ν is Poisson's ratio, λ_G is a screening length, ϵ_0 is the permittivity of free space, ϵ_L is the dielectric constant, R is the radius around the core of the central ion where its pseudopotential is taken as zero (for $R=0$ in practice the approximation above follows), and $J_1(x)$ is the first order Bessel function of the first kind. The magnitude of Eq. 1 was plotted above the x - y plane as shown in Fig. 23 for values of x ranging from -1 to +1 and values of y ranging from -1 to +1 where $(r/\lambda_G)^2 = x^2 + y^2$ and $\theta = \tan^{-1}(y/x)$.

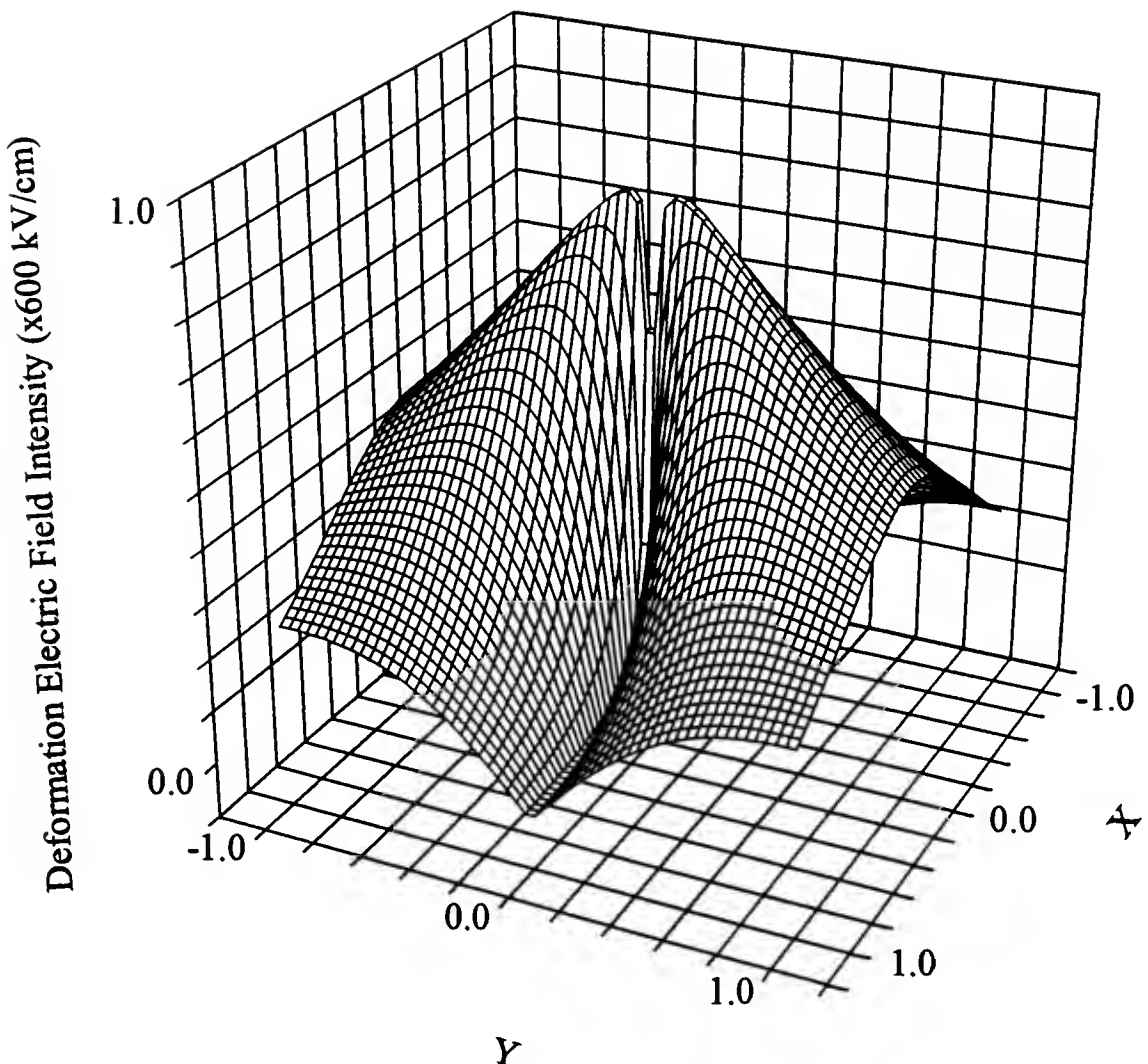


Figure 23 A cartesian mesh plot of the function presented in Eq. 1 showing the electric field intensity due to the deformation potential as a function of position around the dislocation core. The dislocation core lies along the electric field intesity axis.

The scalar coefficient in the Eq. 1 was found to be ~ 600 kV/cm for ZnSe, this value being derived by considering the parameters presented in table 1.

Charged Dislocation Potential

A potential can be developed due to the presence of dangling or unsatisfied bonds in the core of a dislocation. Specifically, if a bond is considered to be occupied by one ground state electron, it can either accept another electron or it can donate the ground state electron to the crystal. This process can result in a net negative or positive line charge depending upon the degree to which the dislocation donates or accepts electrons. Schroter³⁹ first modeled the electric field resulting from charged carriers trapped on a dislocation line and later, Vignaud and Farvacque³⁵ presented a refined form of the model as shown in Eq. 2.

$$E_{cd}(r) = \frac{ef}{2\pi\epsilon_0\epsilon_L b\lambda_G} K_1(r/\lambda_G) \quad (2)$$

where f is the dislocation states occupancy ratio, b is the Burgers vector, and $K_1(x)$ is the first order modified Bessel function of the second kind.

Table 1 ZnSe material parameters necessary to evaluate the scalar coefficient of the microelectric field induced by the deformation potential (Eq. 1).

Parameter	Value
N (m^{-3})	4.39×10^{28}
b_c (m)	3.47×10^{-10}
ν	~ 0.33
ϵ_L	5.92

^afor an ideal 60° dislocation

^b $\epsilon = n^2$ where $n = 2.434$ for ZnSe at 632.8nm

Again, Eq. 2 was plotted above the x-y plane as shown in Fig. 24 for values of x and y ranging as before.

As before, the scalar component of Eq. 2 was found to equal ~ 120 kV/cm for ZnSe, this value being derived from the parameter values shown in table 2.

Piezoelectric Potential

In non-centrosymmetric compounds such as materials having the zincblende crystal structure,⁴⁰ the long range strain fields associated with dislocations in this class of compounds induces an electric polarity within the crystalline lattice via the piezoelectric effect. The expression of the Fourier transform of the total piezo-potential was first calculated by Vignaud and Farvacque⁴¹ and later, the expression was refined by the same authors³⁸ which allowed the piezoelectric field to be expressed in real space as shown in Eq. 3.

$$E_{\text{piezo}}(\theta) = \frac{e_{14} b_c}{2\pi\sqrt{6}(1-v)\epsilon_0\epsilon_L\lambda_G} \frac{f_2(\theta)I_2(r/\lambda_G) + f_4(\theta)I_4(r/\lambda_G)}{r/\lambda_G} \quad (3)$$

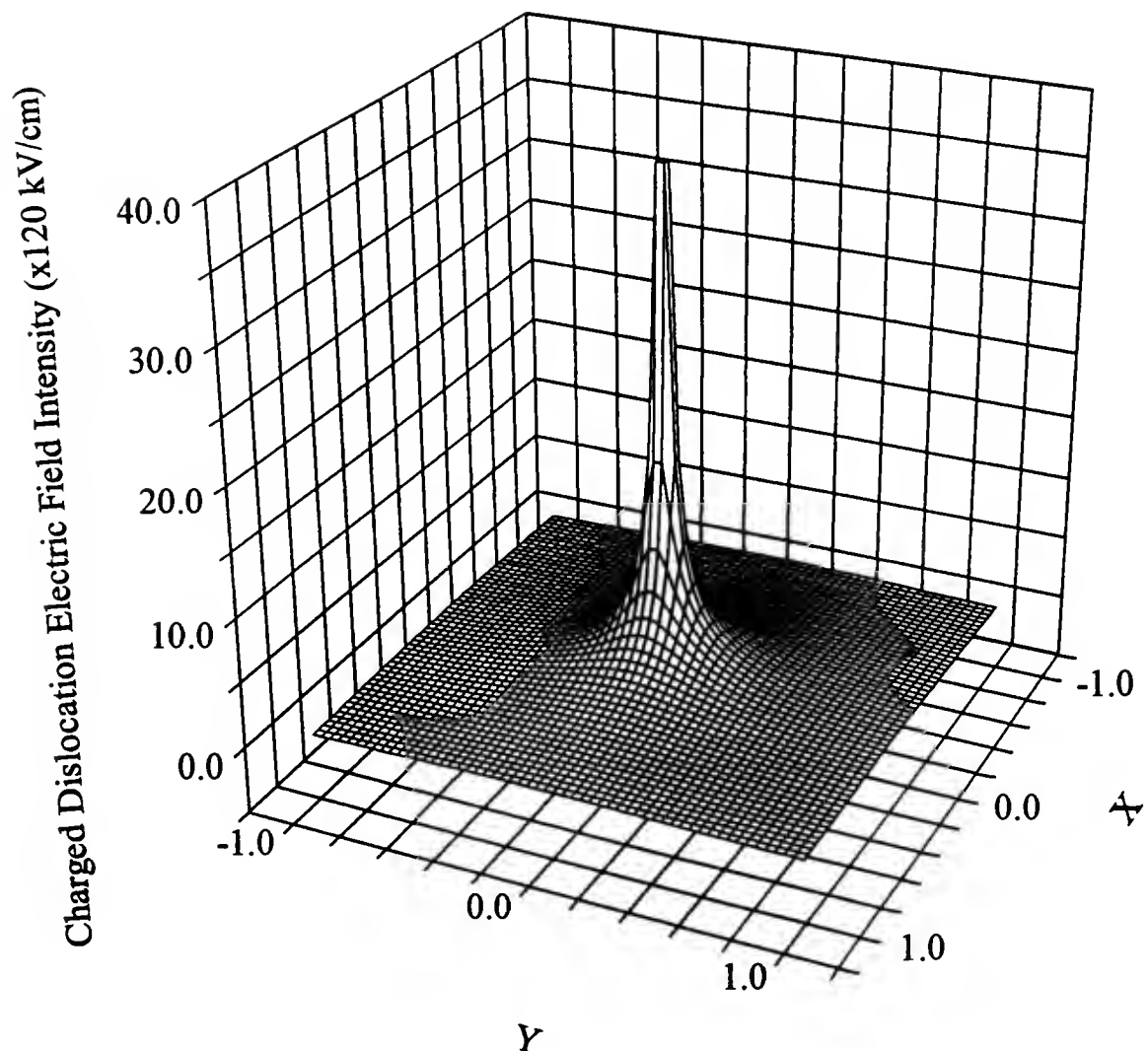


Figure 24 A cartesian mesh plot of the function presented in Eq. 2 showing the electric field intensity due to a charged dislocation as a function of position around the dislocation core. The dislocation core lies along the electric field intensity axis.

Table 2 ZnSe material parameters necessary to evaluate the scalar coefficient of the microelectric field induced by the charged dislocation potential (Eq. 2). GaAs material parameters are used in some cases (denoted by a superscript a) since values for ZnSe were unavailable.

Parameter	Value
f (electron/site)	$\sim^a 0.1$
λ_G (m)	$\sim^a 100 \times 10^{-10}$
b (m)	$^b 4.01 \times 10^{-10}$

^aVignaud and Farvacque³⁵

^bfor an ideal 60° dislocation

where

$$f_2(\theta) = \frac{1-2\nu}{2} \sin(2\theta) + \frac{1+\nu}{\sqrt{2}} \cos(2\theta)$$

$$I_i(r/\lambda_G) = \int_0^{\infty} \frac{K^2 J_i(K)}{K^2 + (r/\lambda_G)^2} dK \approx \frac{1}{a_i + b_i(r/\lambda_G) + c_i(r/\lambda_G)^2}$$

$$f_4(\theta) = \frac{1}{4} \sin(4\theta) + \frac{5}{4\sqrt{2}} \cos(4\theta)$$

and where e_{14} is the piezo-modulus, $a_2=a_4=1$, $b_2=0.04$, $b_4=0.2$, $c_2=0.001$, and $c_4=0.064$. As before, Eq. 3 was plotted as shown in Fig. 25 over the same domain as before.

Lastly, the scalar coefficient in Eq. 3 was found to be ~ 60 kV/cm for ZnSe, this value being derived with e_{14} assumed to be ~ 0.1 C/m² (ref 38).

In summary, the magnitudes of the electric microfields near the core of a dislocation are large, on the order of 10 to 300 kV/cm when evaluated at $r=\lambda_G$ and $\theta=90^\circ$, these values increasing with increasing proximity to the

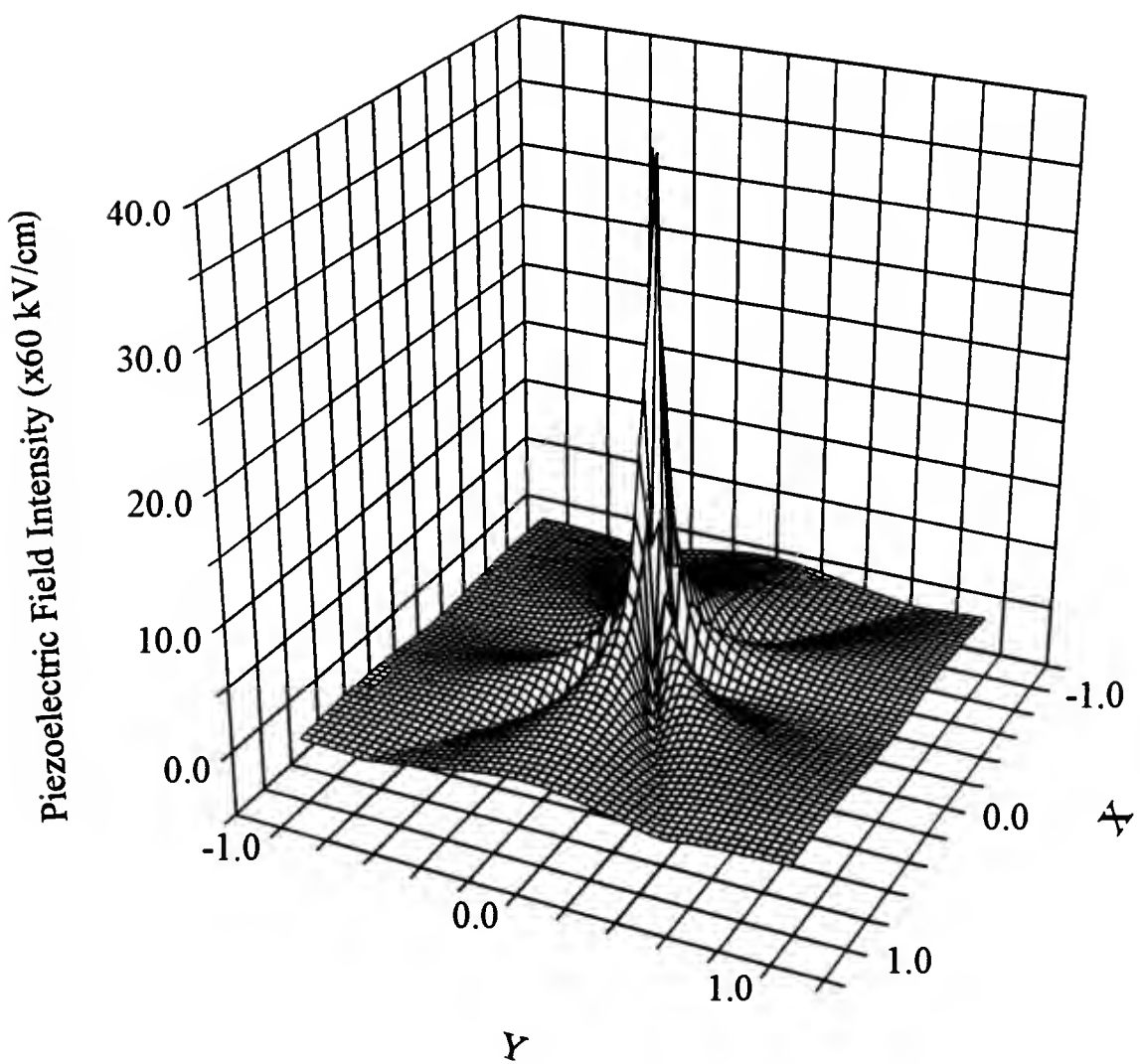


Figure 25 A cartesian mesh plot of the function presented in Eq. 3 showing the piezoelectric field intensity as a function of position around the dislocation core. The dislocation core lies along the electric field intesity axis.

dislocation's core (see Figs. 22-24). Furthermore, the deformation electric field is also largest in magnitude and extent (compare Figs. 23-25) which may make the deformation potential largely responsible for the observed scattering. It is interesting to note that Moriya,⁴² has theoretically predicted and experimentally confirmed that scattering by dislocations in sapphire crystals could be sufficiently explained by considering the changes in the dielectric constant as a consequence of the strain fields around the dislocations, which would tend to support the present hypothesis.

As a final note, it should be mentioned that, since in some cases (as noted) parameter values for ZnSe were not available, known GaAs parameter values were used in order that our calculations could be performed.

The Linear Electro-optic Effect

In semiconductors (such as ZnSe) which are normally optically isotropic, the presence of an electric field induces biaxial birefringence which means that the refractive index in the direction of the field is unaltered while the refractive indices in the transverse directions are changed by Δn .⁴³ This is known as Pockels effect or the linear electro-optic effect and the magnitude of Δn can be described by the function given in Eq. 4.

$$\Delta n(E) = \frac{n^3}{2} r E \quad (4)$$

where n is the refractive index of the material (2.434 for ZnSe at 632.8nm), r is the electro-optic coefficient ($\sim 2 \times 10^{-7}$ cm/kV for ZnSe),⁴⁴ and E is the magnitude of the electric field which, in this case, can range from 10 to 300 kV/cm as stated earlier. It is interesting to note that the magnitudes of these fields are comparable to those employed during electroabsorption and electro-optic modulation in ZnSe/ZnS_{0.92}Se_{0.08} waveguides⁴⁴ (30-40kV/cm) which would tend to support the hypothesis.

Using the values above, Δn is found to range from $\sim 1.4 \times 10^{-5}$ to $\sim 4.3 \times 10^{-4}$, which represents a significant perturbation of the refractive index local to the dislocation's core. Recalling that the field extends to approximately λ_G (which is on the order of 100Å), a dislocation could be modeled as a filament with radius $\sim \lambda_G$ and refractive index $n + \Delta n$. A mass ensemble of such objects (i.e., the dislocation substructure) could then account for the observed scattering of laser light near the heterointerface as postulated earlier.

Conclusions

To conclude, on account of the present theoretical analysis, the refractive index perturbations required to produce the observed laser light scattering at ZnSe/GaAs heterointerfaces could adequately be a consequence of microelectric fields present around the heterointerface defects.

CHAPTER 5 CONCLUSIONS

An *in situ* GaAs surface cleaning process was developed using a remote H atom flux supplied by a UHV compatible rf plasma source. GaAs surface cleanliness and morphology were monitored *in situ* and in real-time using RHEED and a laser light scattering technique, respectively.

From RHEED observations, GaAs surfaces were found to readily clean at temperatures near 350°C using the H atom treatment as opposed to the conventional thermal treatment which requires temperatures near 600°C. The atomically clean GaAs surfaces were found to be specular, as evidenced by laser light scattering observations, when prepared using the H atom treatment. RHEED observations also suggested that hydrogen stabilization of the GaAs surface occurred, the stabilization effect being reversible as evidenced by the observation of a reversible surface reconstruction via RHEED. Although not investigated, it is suggested that future work be performed to elucidate the influence of this phenomena on interface states, initial growth mode, etc. in the subject ZnSe/GaAs material system. Finally,

the key aspect of this portion of the work was that the provision of smooth, specular GaAs surfaces was a necessary prerequisite for subsequent laser scattering measurements during heteroepitaxy since it was important that any scattering be attributed to epitaxy and not a rough GaAs surface.

The laser light scattering (at $\lambda=632.8\text{nm}$) characteristics of undoped ZnSe/(100)GaAs epilayers have been studied *in situ*, in real-time during MBE growth and it has been shown that a laser light scattering signal originates near the heterointerface in these films, as opposed to their free surfaces, when the film thickness exceeds the critical thickness. Specifically, a near-normal incidence HeNe laser probe was employed during epitaxial deposition of ZnSe/GaAs epilayers, the laser probe generating both a specularly reflected signal as well as nonspecular signals. By monitoring both the intensity of laser light scattered into a particular direction (10° away from the incident/reflected beam) and the intensity of the specularly reflected laser light simultaneously, it was observed that the relative temporal phasing between the signals was π . Such an observation suggested (based on an optical ray tracing model) that the source of scattering was located within the film. In support of this conclusion, scanning electron microscopy

observations revealed smooth, featureless film surfaces which would seem to rule out the possibility of significant surface scattering.

Similar experiments were carried out on a very thick ZnSe/(100)GaAs epilayer and it was observed that the relative signal phasing in this case was 0, rather than π , which is consistent with predictions derived from the optical ray tracing model when surface scattering is considered. Thus, it is concluded that a relative temporal phasing of π between the two signals is indicative of a source of scattering within the epilayer itself.

From theoretical considerations, it is postulated, in fact, that the dislocations arising at the ZnSe/(100)GaAs heterointerface as a consequence of strain relief act as laser light scatterers and these defects are therefore the source of the observed scattering. The theory in question suggested that strong microelectric fields surround the resultant defects and perturb the refractive index (via the electro-optic effect) in a localized manner. It is postulated that the collective ensemble of such perturbations is sufficient to scatter the laser light incident on a ZnSe/(100)GaAs heterointerface. Calculations indicated that the field intensities near typical dislocations are around 10-300kV/cm.

To further support the theoretical model, however, post-growth, *ex situ* structural characterization (transmission electron microscopy) was performed on a selection of ZnSe/(100)GaAs heterostructures in an effort to correlate the optical data with the defect structure near the ZnSe/(100)GaAs heterointerface. In general, the structural data mirrored the optical data in that both the amount of defects (evaluated qualitatively) and the intensity of scattering increased with increasing film thickness, leveling off after 500nm of ZnSe had been deposited. Furthermore, the optical data was also sensitive to the type of defect structure occurring near the heterointerface, the type of defect structure being dependent on the source of the GaAs substrate material. Thus, in conclusion, the high degree of correlation observed between the laser light scattering data and the defect structure near the heterointerface supports the theoretical findings concerning the laser light scattering potential of misfit related defects in the ZnSe/(100)GaAs material system.

It can be further concluded that given conditions where a π phase difference is present, the optical probe is indeed monitoring the heterointerface as opposed to the free surface, suggesting the optical probing technique to be eminently suitable for monitoring defect evolution (near the

heterointerface) in such films. Furthermore, it can be concluded that should perfectly lattice-matched structures be grown (i.e., defect-free material), laser light scattering should not be observed during growth which could have important consequences for the provision of lattice-matched structures for widegap II-VI/GaAs diode lasers, for instance.

REFERENCE LIST

1. R.H. Hartley, M.A. Folkard, D. Carr, P.J. Orders, D. Rees, I.K. Varga, V. Kumar, G. Shen, T.A. Steele, H. Buskes and J.B. Lee, *J. Vac. Sci. Technol. B* **10**, 1410 (1992).
2. G.N. Maracas, J.L. Edwards, K. Shiralagi, K.Y. Choi, R. Droopad, B. Johs and J.A. Woolam, *J. Vac. Sci. Technol. A* **10**, 1832 (1992).
3. W.E. Quinn, D.E. Aspnes, M.J.S.P. Brasil, M.A.A. Pudensi, S.A. Schwarz, M.C. Tamargo, S. Gregory and R.E. Nahory, *J. Vac. Sci. Technol. B* **10**, 759 (1992).
4. C.M. Rouleau and R.M. Park, *Appl. Phys. Lett.* **60**, 2723 (1992).
5. C. Lavoie, S.R. Johnson, J.A. Mackenzie, T. Tiedje and T. van Buuren, *J. Vac. Sci. Technol. A* **10**, 930 (1992).
6. A.J. Pidduck, D.J. Robbins, A.G. Cullis, D.B. Gasson and J.L. Glasper, *J. Electrochem. Soc.* **136**, 3083 (1989).
7. A.J. Pidduck, D.J. Robbins, D.B. Gasson, C. Pickering and J.L. Glasper, *J. Electrochem. Soc.* **136**, 3088 (1989).
8. D.J. Robbins, A.G. Cullis and A.J. Pidduck, *J. Vac. Sci. Technol. B* **9**, 2048 (1991).
9. J.P. Contour, J. Massies, A. Salettes and P. Staib, *Appl. Phys. A* **38**, 45 (1985).
10. R.P. Vasquez, B.F. Lewis and F.J. Grunthaner, *Appl. Phys. Lett.* **42**, 293 (1983).

11. J.P. Contour, J. Massies, A. Salettes, M. Outrequin, F. Simondet and J.F. Rochette, *J. Vac. Sci. Technol. B* **5**, 730 (1987).
12. M. Hirose, S. Yokoyama and Y. Yamakage, *J. Vac. Sci. Technol. B* **3**, 1445 (1985).
13. R.P.H. Chang, C.C. Chang and S. Dirack, *J. Vac. Sci. Technol. B* **20**, 45 (1982).
14. A. Takamori, S. Sugata, K. Asakawa, E. Miyauchi and H. Hashimoto, *Jpn. J. Appl. Phys.* **26**, L142 (1987).
15. S. Sugata, A. Takamori, N. Takado, K. Asakawa, E. Miyauchi and H. Hashimoto, *J. Vac. Sci. Technol. B* **6**, 1087 (1988).
16. P. Friedel and J. Landesman, *Philos. Mag. B* **55**, 711 (1987).
17. Z. Lu, M.T. Schmidt, D. Chen and R.M. Osgood Jr., *Appl. Phys. Lett.* **58**, 1143 (1991).
18. M. Cherchour, F. Proix and C. Sebenne, *Rev. Phys. Appl.* **22**, 285 (1987).
19. J.A. Schaefer, V. Persch, S. Stock, Th. Allinger and A. Goldmann, *Europhys. Lett.* **12**, 563 (1990).
20. E.J. Petit, F. Houzay and J.M. Moison, *J. Vac. Sci. Technol. A* **10**, 2172 (1992).
21. E.J. Petit and F. Houzay, *J. Vac. Sci. Technol. B* **12**, 547 (1994).
22. R.M. Park, *J. Vac. Sci. Technol. A* **10**, 701 (1992).
23. B.W. Shore and D.H. Menzel, *Principles of Atomic Spectra* (Wiley, New York, 1968).
24. R.M. Park, M.B. Troffer, C.M. Rouleau, J.M. DePuydt and M.A. Haase, *Appl. Phys. Lett.* **57**, 2127 (1990).

25. T.B. Massalski, H. Okamoto, P.R. Subramanian and L. Kacprzak, Eds., *Binary Alloy Phase Diagrams*, vol. 1 (ASM International, Materials Park, OH, 1990).
26. P. O'Keeffe, C. O'Morain, S. Komuro, M. Ishii, T. Meguro, Y. Iimura, S. Den, T. Morikawa and Y. Aoyagi, *Jpn. J. Appl. Phys.* **31**, 3301 (1992).
27. K. Ohkawa, T. Karasawa and T. Mitsuyu, *Jpn. J. Appl. Phys.* **30**, L152 (1991).
28. H. Okuyama, T. Miyajima, Y. Morinaga, F. Hiei, M. Ozawa and K. Akimoto, *Electron. Lett.* **28**, 1798 (1992).
29. M.A. Haase, J. Qiu, J.M. DePuydt and H. Cheng, *Appl. Phys. Lett.* **59**, 1272 (1991).
30. H. Jeon, J. Ding, W. Patterson, A.V. Nurmikko, W. Xie, D.C. Grillo, M. Kobayashi and R.L. Gunshor, *Appl. Phys. Lett.* **59**, 3619 (1991).
31. J.R. Vig, *J. Vac. Sci. Technol. A* **3**, 1027 (1985).
32. S. Ingrey, W.M. Lau and N.S. McIntyre, *J. Vac. Sci. Technol. A* **4**, 984 (1986).
33. J.M. Olson and A. Kibbler, *J. Cryst. Growth* **77**, 182 (1986).
34. J. Kleiman, R.M. Park and S.B. Qadri, *J. Appl. Phys.* **61**, 2067 (1987).
35. D. Vignaud and J.L. Farvacque, *J. Appl. Phys.* **65**, 1261 (1989).
36. J.D. Dow, *Phys. Rev. B* **5**, 594 (1972).
37. J.L. Farvacque and P. Lenglart, *Phys. Status Solidi B* **80**, 361 (1977).
38. D. Vignaud and J.L. Farvacque, *J. Appl. Phys.* **67**, 281 (1990).
39. W. Schroter, *Phys. Status Solidi A* **19**, 159 (1973).

40. M.E. Lines and A.M. Glass, *Principles and Applications of Ferroelectrics and Related Materials* (Clarendon Press, Oxford, 1977).
41. D. Vignaud and J.L. Farvacque, *Phys. Status Solidi B* **125**, 785 (1984).
42. K. Moriya, *Philos. Mag. B* **64**, 425 (1991).
43. J.I. Pankove, *Optical Processes in Semiconductors* (Dover, New York, 1971).
44. M.H. Jupina, E.M. Garmire, N. Shibata and S. Zembutsu, *IEEE J. Quan. Elect.* **28**, 663 (1992).

BIOGRAPHICAL SKETCH

Christopher M. Rouleau was born on March 23, 1966, in Springfield, Massachusetts. He attended school in Hampden, Massachusetts, and graduated from Minnechaug Regional High School (Wilbraham, Massachusetts) in 1984.

He entered Western New England College (WNEC) in Springfield, Massachusetts, that same year to pursue a degree in electrical engineering and qualified for the dean's list every semester. While attending WNEC, he received a number of awards, including the 1986 Sophomore Academic Award, the 1986 Kenneth A. Macleod Scholarship Award, and the 1987 and 1988 Electrical Engineering Departmental Awards. Christopher graduated in 1988 from Western New England College with a Bachelor of Science in Electrical Engineering degree. His superior academic achievement was recognized at graduation as he was not only awarded the honor of summa cum laude but was also given special recognition for attaining the highest cumulative grade point average among graduating seniors.

In the fall of 1988, Christopher came to the University of Florida to pursue a master's degree in materials science and engineering. In 1991 he earned that degree; his thesis, conducted under the direction of Professor Robert M. Park, was titled Growth by Molecular Beam Epitaxy and Electrical Characterization of Cl-doped ZnSe/(100)GaAs Epitaxial Layers.

While at the University of Florida, Christopher continued his pursuit of excellence. He was awarded first prize in the 1992 Student Poster Competition at the 21st Annual Symposium on Applied Vacuum Science and Technology, the 1991 Outstanding Bent Award (Tau Beta Pi, Florida alpha chapter), and the prestigious 1993 Materials Research Society Graduate Student Award.

Christopher is currently an active member of four honor societies (Sigma Beta Tau, Tau Beta Pi, Phi Kappa Phi, and Alpha Sigma Mu) and two professional societies (American Vacuum Society and Materials Research Society). He has also authored or coauthored 11 publications to date and has presented papers at three national meetings.

Christopher plans to pursue a postdoctoral appointment at Oak Ridge National Laboratory (Oak Ridge, Tennessee) that involves the deposition of selected materials via a novel laser-sourced molecular beam epitaxy (Laser-

MBE) technique with a view towards fabrication of high-efficiency photovoltaic cells.

I certify that I have read this study and that in my opinion it conforms to acceptable standards of scholarly presentation and is fully adequate, in scope and quality, as a dissertation for the degree of Doctor of Philosophy.



Robert M. Park, Chairman
Professor of Materials
Science and Engineering

I certify that I have read this study and that in my opinion it conforms to acceptable standards of scholarly presentation and is fully adequate, in scope and quality, as a dissertation for the degree of Doctor of Philosophy.



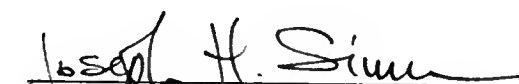
Paul H. Holloway
Professor of Materials
Science and Engineering

I certify that I have read this study and that in my opinion it conforms to acceptable standards of scholarly presentation and is fully adequate, in scope and quality, as a dissertation for the degree of Doctor of Philosophy.



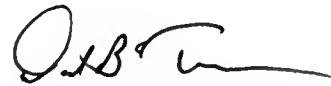
Kevin S. Jones
Associate Professor of Materials
Science and Engineering

I certify that I have read this study and that in my opinion it conforms to acceptable standards of scholarly presentation and is fully adequate, in scope and quality, as a dissertation for the degree of Doctor of Philosophy.



Joseph H. Simmons
Professor of Materials
Science and Engineering

I certify that I have read this study and that in my opinion it conforms to acceptable standards of scholarly presentation and is fully adequate, in scope and quality, as a dissertation for the degree of Doctor of Philosophy.



David B. Tanner
Professor of Physics

This dissertation was submitted to the Graduate Faculty of the College of Engineering and to the Graduate School and was accepted as partial fulfillment of the requirements for the degree of Doctor of Philosophy.

August, 1994



Winfred M. Phillips
Dean, College of Engineering

Karen A. Holbrook
Dean, Graduate School

LD
1780
1994
. R 859

UNIVERSITY OF FLORIDA



3 1262 08553 7032